January 2018

Study Of Physical And Chemical Properties Of Iridium Modified Nanostructures Formed On Silicon (110) Surface

Rasika Mohottige

STUDY OF PHYSICAL AND CHEMICAL PROPERTIES OF IRIDIUM MODIFIED NANOSTRUCTURES FORMED ON SILICON (110) SURFACE

by

Rasika Nishantha Mohottige
Bachelor of Science, Open University of Sri Lanka, 2007
Master of Philosophy in Physics, Open University of Sri Lanka, 2012

A Dissertation

Submitted to the Graduate Faculty

of the

University of North Dakota

in partial fulfillment of the requirements

for the degree of

Doctor of Philosophy

Grand Forks, North Dakota
May
2018

This dissertation submitted by Rasika N Mohottige in partial fulfillment of the requirements for the Degree of Doctor of Philosophy from the University of North Dakota has been read by the Faculty Advisory Committee under whom the work has been done and is hereby approved.

Dr. Nuri Oncel

Dr. Kanishka Marasinghe

Dr. Yen Lee Loh

Dr.Graeme Dewar

Dr. Mark Hoffmann

This dissertation is being submitted by the appointed advisory committee as having met all of the requirements of the School of Graduate Studies at the University of North Dakota and is hereby approved.

Grant McGimpsey
Dean of the School of Graduate Studies

April 23, 2018
Date

PERMISSION

Title Study of physical and chemical properties of nanostructures formed on Ir modified Si (110) surface

Department Physics and Astrophysics

Degree Doctor of Philosophy

In presenting this dissertation in partial fulfillment of the requirements for a graduate degree from the University of North Dakota I agree that the library of this University shall make it freely available for inspection. I further agree that permission for extensive copying for scholarly purposes may be granted by the professor who supervised my dissertation work or in his absence by the chairperson of the department or the dean of the Graduate School. It is understood that any copying or publication or other use of this dissertation or part thereof for financial gain shall not be allowed without my written permission. It is also understood that due recognition shall be given to me and to the University of North Dakota in any scholarly use which may be made of any material in my dissertation.

Rasika N Mohottige
May 12, 2018

TABLE OF CONTENTS

LIST OF FIGURES

FIGURE PAGE

LIST OF ACRONYMS

1D	One Dimensional
ARPES	Angle Resolve Photoemission Spectroscopy
E_F	Fermi Energy
HOMO	Highest Occupied Molecular Orbital
LDOS	Local Density of States
LEED	Low Energy Electron Diffraction
LUMO	Lowest Occupied Molecular Orbital
MBE	Molecular Beam Epitaxy
ML	Monolayer
NW	Nanowires
QD	Quantum Dot
RHEED	Reflection High Energy Electron Diffraction
STM	Scanning Tunneling Microscopy
STS	Scanning Tunneling Spectroscopy
TEM	Transmission Electron Microscopy
UHV	Ultra High Vacuum
XPS	X-Ray Photoelectron Spectroscopy

ACKNOWLEDGEMENTS

I wish to express my sincere appreciation for my research advisor Associate Professor.Dr. Nuri Öncel; his fair approach to both life and work has undoubtedly been the reason that I learned and succeeded as much as I have. I also take this opportunity to express my gratitude for how much time and effort that he has spent one-on-one with me to show and teach me everything about solid-state physics research and at times life in general.

As for my graduate studies, I would like to thank Dr. Kanishka Marasinghe Dr. Mark Hoffmann Dr.Yen Lee Loh and Dr.Graeme Dewar for serving in my dissertation committee. I would also like to thank the rest of the Department of Physics faculty for their constant support throughout my graduate studies and Rob Czapiewski for his talents and hard work to help maintain our laboratory equipment.

Finally, I would like to thank all my colleagues for their friendship and vital research contributions to each project in this dissertation and Dr.Soumya Bernerjee who made suggestions and comments on my dissertation to make it better.

I would like to dedicate this dissertation to my ever-loving grandmother Anulawathi Sedar Mohottige my son Chamathka and Senul Sedar Mohottige my loving wife Indu Mohottige and my parents Nimal and Kusumlatha Sedar Mohottige.

ABSTRACT

Scanning Tunneling Microscopy and Spectroscopy (STM/STS), Transmission Electron Microscopy (TEM), and X-Ray Photoelectron Spectroscopy (XPS) studies were performed to characterize the morphology, electronic properties, and chemical properties of the Iridium (Ir) induced nano-structures formed on clean Si (110) surface. It was found that the deposition of Ir in the sub-monolayer and monolayer (ML) regime on clean Si (110) ``16 × 2'' surface produces Ir-silicide nano-structures, as this surface is suitable for growing nanostructures because of its inherent structural asymmetry. STM shows that nanowires with an average length and width of 100 nm and 21 nm, respectively, were grown on clean Si (110) surface when 0.25 ML of Ir was deposited. Statistical analysis of STM images of Ir-silicide nanowires show that the length and the width of the nanowires are correlated. TEM results show that there are two different regions across the nanowires, one close to the Si substrate which is made of $IrSi_2$ and other close to the nanowire surface which is possibly made of amorphous Ir. STS indicates that the nanowires have different electronic properties. The smaller nanowires are metallic based on size, but the bigger nanowires are semiconducting with a band gap of ~ 0.34 eV.

STM images indicate that 2 ML of Ir deposition produces Ir covered flat terraces on clean Si (110). The interface between the Ir and substrate is Ir-silicide.

In addition, quasi periodic Ir quantum dots (QDs) appear on Ir terraces. Quantum dots are loosely bound to the terraces as they tend to move around if the STM tip comes close to them. STS indicates that Ir-QDs exhibit Coulomb blockade and a negative differential resistance at room temperature. Coulomb blockade and a negative differential resistance in the dI/dV plot indicates a Coulomb gap of ~ 0.7 eV.

XPS data shows that the binding energy of both Ir modified Si $2p_{3/2}$ and Si modified Ir $4f_{7/2}$ peaks shift towards higher energy with respect to pure Si and Ir which indicates that the interface between Ir terrace and the Si substrate has a Si rich silicide layer.

CHAPTER I

INTRODUCTION

Surface science studies physics and chemistry at the interface of two phases including solid-liquid solid-gas solid-vacuum and liquid-gas interfaces. Over the years many different surface science techniques have developed and a vast amount of knowledge about surface science has been accumulated[1]. Due to countless possibilities for various device applications surfaces and interfaces have always drawn attention from scientists coming from various disciplines ranging from basic to applied sciences. By looking at how electronics evolve it is safe to claim that importance of surfaces and interfaces will keep growing. Soon we will reach to a level where we will be building devices that solely rely on physical and electronic properties of structures that have a thickness of up to a few-nanometers. In fact, Intel's 14 nm process and lead system-on-a-chip product have already been qualified and in volume production with fabs in Oregon (2014) Arizona (2014) and Ireland (2015)[2].

According to Moore's law the number of transistors on an integrated circuit doubles every eighteen months. This kind of progress is possible if the size of individual transistors can be scaled down in a cost-efficient way. However, this trend cannot continue forever. There are two important obstacles that can prevent further scaling down.

The first one is about physical limitations such as nano-scale variations in dopant concentrations enhanced leakage at short gate lengths etc. The second one is the lack of new technologies to manufacture well defined and well-organized components in nanometer size. Therefore, a new approach is required to overcome all these limitations. This new approach is called bottom-up approach which utilizes the concepts of self-assembly to build individual components of an integrated circuit. In my thesis I focused on two types of self-assembled structures nanowires and quantum dots. I used various characterization techniques such as Scanning Tunneling Microscopy/Spectroscopy (STM/STS) X-ray Photoelectron Spectroscopy (XPS) and Low Energy Electron Diffraction (LEED) to study physical and electronic properties of these systems.

1.1: Silicon (Si) and Silicon surfaces

Si has 14 electrons ten of which fill the first three orbitals (1s 2s 2p) and the remaining four electrons partially occupy 3s 3p orbitals. The 3s and 3p orbitals are hybridized to form four tetrahedral sp^3 orbitals.

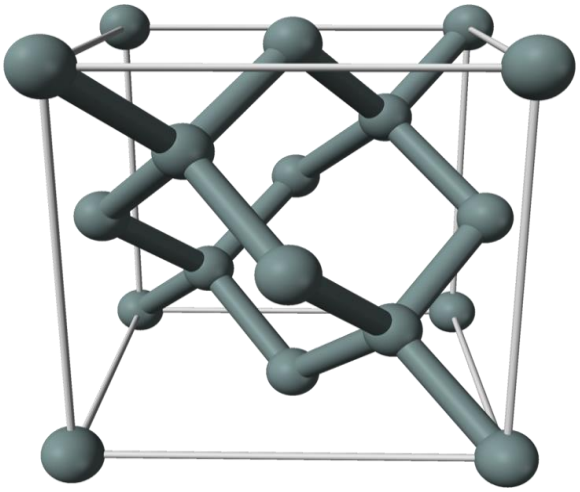

Figure 1.1 A model of a bulk Si crystal

In bulk each Si atom has four nearest neighbors and the lattice constant of the crystal is 5.431 Å. The space lattice of silicon like diamond is face-centered cubic. The primitive basis of silicon contains two identical atoms at coordinates 000 and $\frac{1}{4}\frac{1}{4}\frac{1}{4}$ with respect to fcc lattice points. The conventional fcc lattice contains 4 lattice points therefore conventional unit cube of silicon contains 8 atoms.

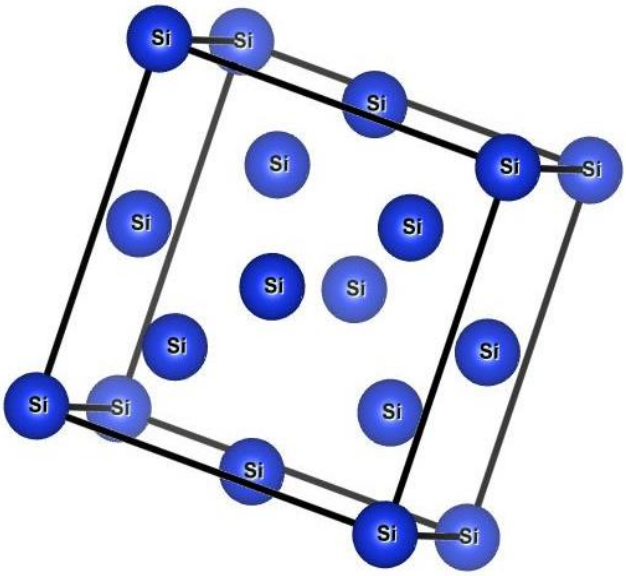

Figure 1.2 A unit cell of bulk Silicon

Each covalent bond has two spin paired electrons. Therefore, when a surface is prepared by cutting the crystal in a specific orientation depending on the specific direction of cutting and the position of the atom one or two bonds of a surface Si atom become free which is called dangling bond. Dangling bonds increases surface energy via reconstruction Si atoms come together and make new bonds to reduce the number of dangling bonds on the surface.

During the relaxation and reconstruction surface atoms are displaced from their bulk position but it preserves the periodicity or symmetry of the surface. Different surfaces of a crystal have different surface free energies depending on their orientations. The most stable surface is the one which exhibits the lowest surface free energy.

1.2: Silicon (Si [110]) surfaces

In comparison of other silicon surfaces such as Si (111) and Si (001) Si (110) surface has received the least amount of attention because of the difficulty of preparing highly anisotropic surface of Si (110). However recently CMOS transistor built on the Si (110) surface received some attention due to the higher hole mobility[3]. In addition to that surfaces with high anisotropy is a good template to grow nanowires which made Si (110) surface an ideal substrate to grow nanowires of different materials[4,5].

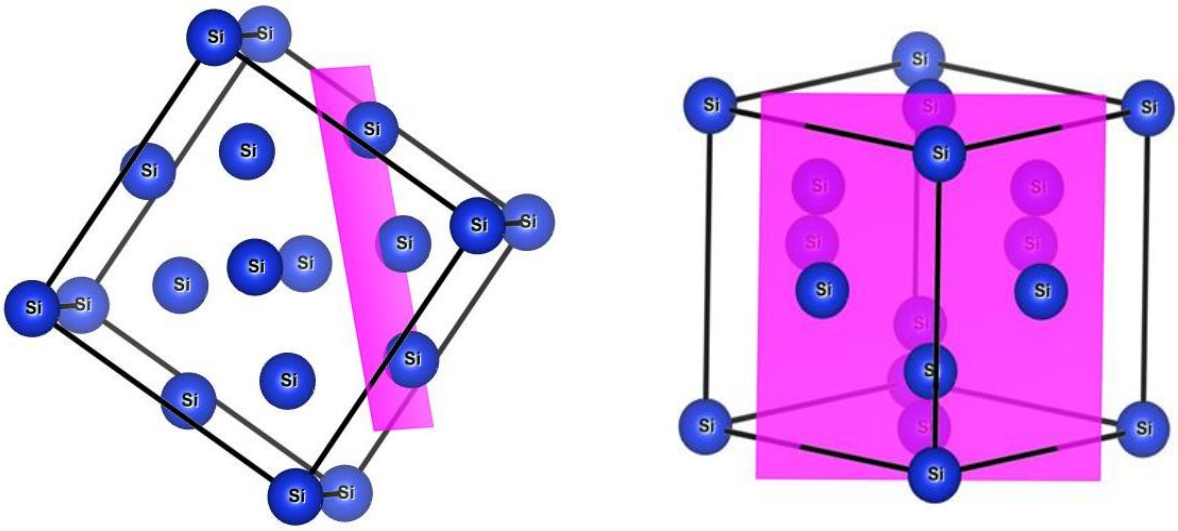

Figure 1.3(a) Si (110) plane (side view) (b)Front view of Si (110)

Various surface reconstruction was observed on clean Si (110) surface such as “1 × 2” “2 × 1” ”1 × 5” “5 × 4” and “16 x 2” [6]. Among those structures “16 × 2’’ is the most famous one. The “16 × 2’’ structure was found in 1980 by using reflection high-energy electron diffraction (RHEED)[7].

Ampo *et al*. made a step structure model for the “16 × 2” structure based on analysis of the LEED pattern. Van Loenen Dijkkamp and Hoeven confirmed it by STM observation. STM observations on Si (110) -(16 × 2) show two predominant patterns one is alternating up and down steps one atomic layer high and ∼5 nm wide running in the [-112] or [1-12] direction[8,9] and a pair of pentagons on both the upper and lower terraces[10]. Several models for the structure of the pentagon have been proposed[11 - 14]. Among them “tetramer-Interstitial” model [Fig1.4] shows that the pentamer is stabilized by the surface self-interstitial. This model clearly shows the pentagon structure consists of tetramer (A and B adatoms) and a substrate atom (open circle labeled as “C”). The atom C protrudes towards the vacuum in the presence of the six-fold coordinated interstitial.

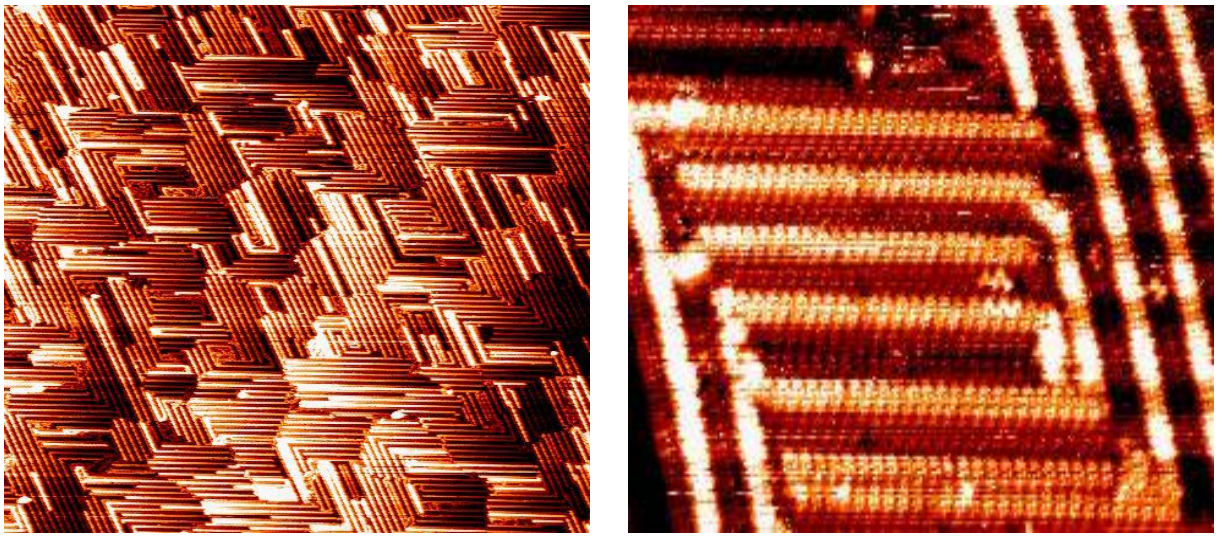

Figure 1.4 Topographic images of a clean Si (110). (a) A wide scan image (90 nm × 90 nm) ;(b) An enlarged image (17 nm × 17 nm) showing the pentagon structure

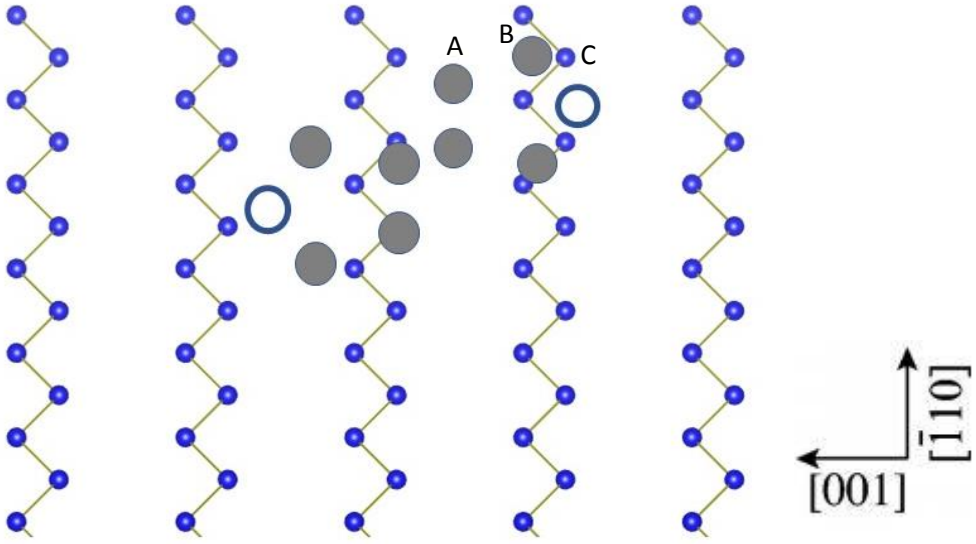

Figure 1.5 Proposed “tetramer Interstitial” model

1.3: Iridium silicide nanowires on Si (110) surface

The transition metal-silicon interface is important both from fundamental science and technological application perspectives. From the fundamental science perspective transition metal-silicon systems provide unique opportunities to investigate heteroepitaxial thin films. Previous studies on various transition metal-silicon systems reveal that these interfaces can exhibit rather novel physical properties such as giant Rashba split bands quantum confinement Peierls instability and Tomonaga-Luttinger liquid. From the technological application perspective metal-semiconductor interfaces are rectifying junctions with various Schottky barrier heights. Among metal-semiconductor interfaces the Ir/Si interface is special because it has the lowest (highest) Schottky barrier for holes (electrons). The initial stages of metal growth are vital for device performance since the Schottky barrier height strongly depends on the interface states between metal and semiconductor. Although there is an extensive literature on the initial stages of growth for almost all metal/silicon systems Ir growth on semiconductor surfaces have not been studied in detail. Our group investigated various Ir modified Si surfaces over the years.

In chapter 3 and 4 I will discuss in detail physical and chemical properties of Ir-silicide nanowires grown on Si (110) surface. As mentioned above Si (110) surface has not been as popular as the other cuts of Si surface but at the same time due to its asymmetric nature Si (110) surface offers unique opportunities to grow nanowires. Nanowires will play an essential role in the future of semiconductor technologies. They will provide connection between individual components of an integrated circuit. There are already some studies on

various materials and fabrication methods that can be used today[17,18]. We want to look beyond what is out there today and focus on what will be needed in the future. We believe that in the future self-assembled nanowires grown on silicon surfaces can be used for various optoelectronic applications.

In chapter 5 metallic Ir quantum dots grown on Ir modified Si (110) will be discussed. A quantum dot is a confined space surrounded by tunneling barriers in all three dimensions. Quantum dots similar to atoms exhibit discrete spectra of energy levels. Therefore, they are also named as artificial atoms. Quantum dots can be metals or semiconductors[19 - 23]. Quantum dots can function like a single electron transistor and exhibit Coulomb blockade. Quantum dots can also be implemented as qubits for quantum computers. We are particularly interested in metallic quantum dots. A relatively high electron density large effective mass and short phase coherence length of a metallic quantum dot allow us to consider only the charging energy of Single Electron Tunneling (SET) to/from the metallic quantum dot.

CHAPTER II

EXPERIMENTAL METHODS

All the experiments in this thesis have been carried out using Scanning tunneling microscopy (STM) X-ray photoemission microscopy (XPS) low energy electron diffraction (LEED) and transmission electron microscopy (TEM) systems and under Ultra-High Vacuum (UHV) conditions. STM LEED and XPS systems are located at UND we traveled to Oak Ridge National Laboratory for TEM experiments. This chapter is an overview of experimental techniques and theoretical background of the experimental methods.

2.1: Ultra high vacuum (UHV) system and Components

While studying the properties of a surface the composition of the surface should remain constant throughout the experiment which means that the rate of arrival of reactive species from the surroundings should be low otherwise sample will be contaminated. To achieve this, it is a common practice to perform experiments under UHV conditions. In order to reach UHV we use various pumps. Both XPS and STM systems have turbo pumps backed by rough pumps and ion pumps equipped with Ti sublimation. Both systems are kept at about $2 \times 10^{-10}\ mbar$ pressure. After venting the system for routine maintenance and repair we bake the systems at 140 ^{0}C for 24 hours to achieve UHV conditions within a reasonable amount of time (2- 3 days).

After a typical bake we performed routine degassing and conditioning of filaments and evaporation sources. A picture of STM / LEED in UHV system is shown in Figure 2.1.

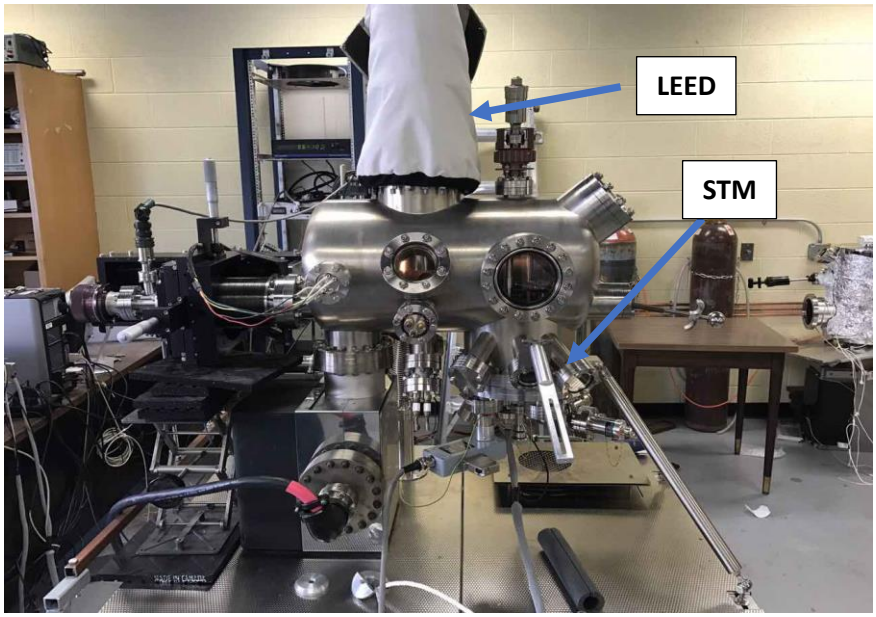

Figure 2.1 UHV system setup with sample preparation chamber with STM and LEED

2.2: Theory of STM

Scanning Tunneling Microscopy (STM) images do not just provide atomic resolution images of surfaces but also it can function as a spectroscopy tool which enable us to study local electronic properties of surfaces with atomic precision. The most crucial part of the STM is the probe tip that is attached to a piezo electric material which consist of three mutually perpendicular piezoelectric transducers in x y z coordinates.

This piezoelectric transducer contract or expand as a function of applied voltage (V) allowing STM tip to move on the surface with sub-angstrom precision. We electrochemically etch tungsten to prepare sharp metallic tips for scanning. The figure 2.2 shows the schematic diagram of STM device.

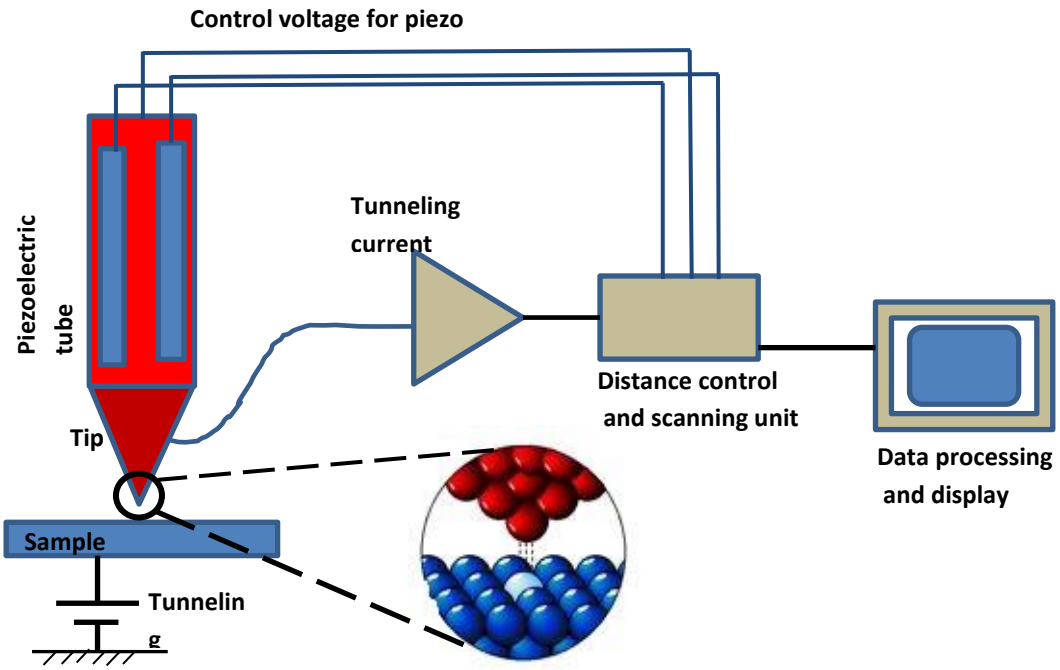

Figure 2.2 Schematic diagram of STM

The basic physics behind the STM is quantum tunneling. In a UHV system potential barrier is the vacuum gap between the tip and the sample. Schematic diagram of the STM in fig (2.2) shows the potential barrier between the sample and the tip. A schematic tip sample electron tunneling in one dimensional system is shown in following figure (2.3).

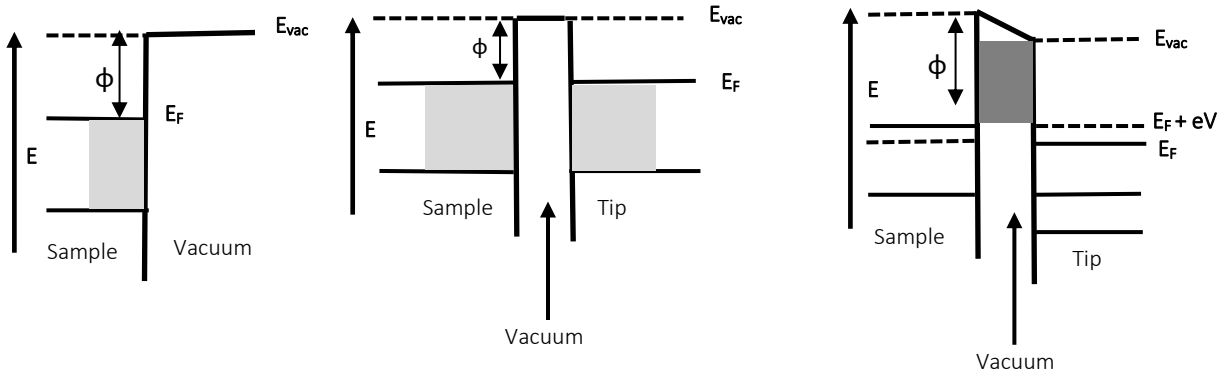

Figure 2.3 1D representation of potential barriers. (a) Non-interacting system with energy E_{VAC}. (b) Tip and sample in equilibrium with common Fermi energies and the difference between work functions is depicted as an electric field in the gap. (c) An applied voltage promotes tunneling between tip and sample where the energies in the gray area can contribute to tunneling.

Using Fermi's golden rule, we can write the current flowing from the tip to the sample and from the sample to the tip as follows

$$I_{t\to s} = \frac{2\pi e}{\hbar} \int |M_{ts}|^2 N_t(E - eV) N_s(E) f_t(E - eV)[1 - f_s(E)] dE \quad (2)$$

$$I_{s\to t} = \frac{2\pi e}{\hbar} \int |M_{ts}|^2 N_t(E - eV) N_s(E)[1 - f_t(E - eV)] f_s(E) dE \quad (3)$$

$$f(E) = \left[\exp\left(\frac{E - E_F}{k_B T}\right) + 1\right]^{-1} = \text{Fermi} - \text{Dirac distribution}$$

N(E) denotes the Density of States. The occupied states ($N_t f_t$) can tunnel into unoccupied sample states (Ns [1 - f_s]). The common energy scale is selected to be that of the sample and thus the tip energy scale is shifted by ΔE = eV.

The total current flowing from the tip to the sample can be written as

$$I = I_{t\to s} - I_{s\to t} = -\frac{2\pi e}{\hbar}\int |M_{st}|^2 N_t(E-eV)N_s(E)[f_s(E) - f_t(E-eV)]dE \quad (4)$$

To analyze electronic properties of the surface we need to get the Local Density of States(LDOS). The LDOS is derived from the STS data that we collected during the measurements. We calculate LDOS by getting the derivative of the tunneling current with respect to sample bias voltage (dI/dV) divided by the absolute value of the conductance (I/V). LDOS is given by

$$LDOS = \frac{\frac{dI}{dV}}{\left|\frac{I}{V}\right|} = \frac{dI}{dV}\left|\frac{V}{I}\right| \quad (5)$$

2.3: Low Energy Electron Diffraction (LEED)

Low energy electron diffraction (LEED) is one of the most powerful technique used in surface analysis. This technique widely used in surface science and material science to study surface structure. This technique operates by sending a collimated beam of electrons from the electron gun to the surface of the sample being tested. An electron gun consists of a heated electron generator (cathode) and set of focusing lenses to send the electron towards the sample surface. Once electrons hit the sample surface they diffract in various

direction according to the surface crystallography of the sample. After electrons diffract from the surface electrons go back towards the three grids followed by a phosphorous screen. The first grid is grounded and serves as a shield which protects the second grid because of its negative potential. The second grid act as a filter which allows only elastically backscattered electrons to pass through. All inelastic electrons are blocked because they create blurred images. Once elastically backscattered electrons pass through the second grid they reach to third grid which separates the negative grid from the phosphorous screen which carries positive charge. As the electrons hit the phosphorous screen electrons create a glowing on the screen. The pattern of the glow represents the atomic arrangement of the crystal structure. Schematic diagram of the LEED is shown below figure (2.4).

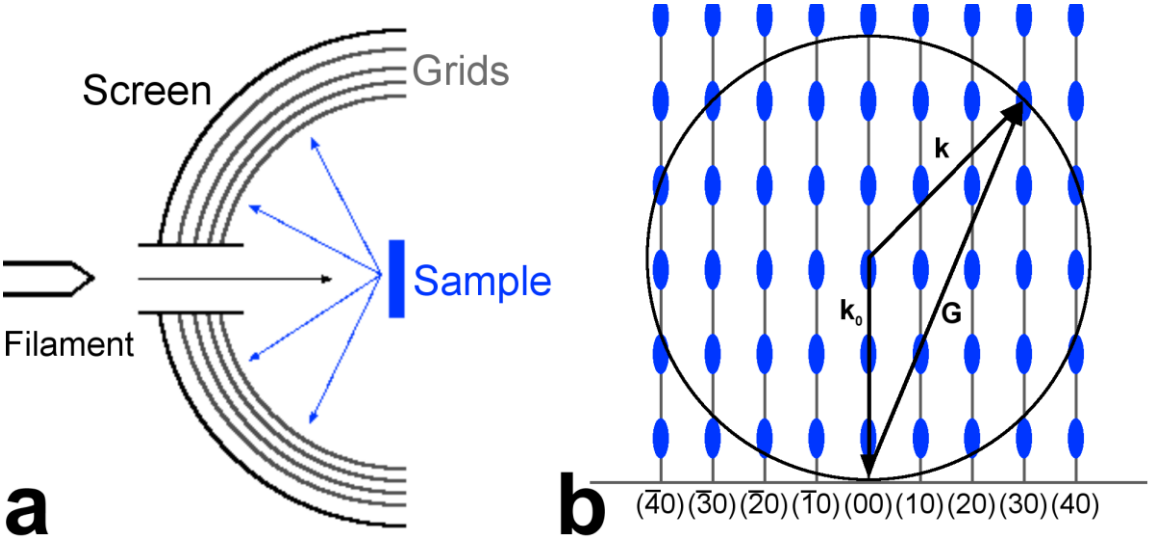

Figure 2.4(a) Schematic of LEED setup with sample. (b) Ewald construction of surface scattering where diffraction pattern is the rods vertical to the surface.

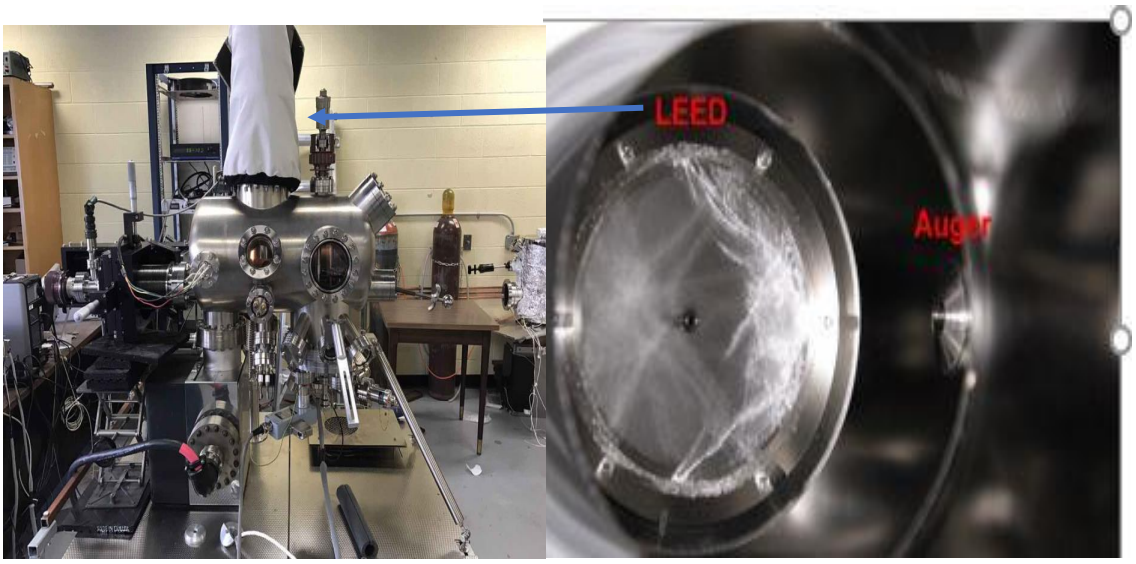

Figure 2.5 (a) UHV set up with LEED (b) LEED screen

To get the diffraction pattern of the crystal surface Laue condition should be satisfied with incident electrons with wave vector $k_0 = 2\pi / \lambda_0$ and the scattered wave vector $k = 2\pi / \lambda$. So, the constructive interference and the diffraction is given by

$$k - k_0 = G_{hkl} \quad (6)$$

Where (hkl) is a set of integers and G_{hkl} is a vector of the reciprocal lattice.

2.4: X-Ray Photoelectron Spectroscopy (XPS)

Photoelectron spectroscopy is a general term that refers to all those techniques based on the application of the photoelectric effect originally explained by Albert Einstein. When light shines on a sample an electron can absorb a photon from the light and escape from the material with some kinetic energy. XPS is a relatively simple technique which we can get vast amount of information about the sample being tested including chemical composition and chemical states. XPS is based on two processes which result due to interaction between x-rays and electrons. The first step is Compton scattering. An incident x-ray collides with a core electron. The collision causes the electron to be ejected from the electronic shell. The electron is released with certain kinetic energy that is directly related to the binding energy of the electron to the atom. The ejection of the inner core electron leads to the second processes that the missing inner core electron represents an unstable hole in the electronic shell. An electron from the valance shell then fills the newly formed hole causing an Auger electron to be emitted from the valance shell to conserve energy.

Again, the kinetic energy of the emitted electron is directly related to the binding energy of the electron to the atom. These two processes are used to identify the elements in the sample since the binding energies of the electrons are unique for every element. To determine the binding energies, we first need to measure the kinetic energies of the emitted electrons. Once the analyzer collects the data we can calculate the binding energies of the electrons if we know the wavelength of the incident x-rays.

$$BE = h\upsilon - KE - \phi_{spec} \tag{7}$$

$$\upsilon = \frac{c}{\lambda} \tag{8}$$

Equations given above show the relationship between the kinetic energy of the emitted electron (KE) and the binding energy (BE) of that particular electron to the atom. The frequency of the incident x-ray (ν) is related to the wavelength (λ) of the x-ray and the speed of light (c) and ϕ_{spec} is the work function of the spectrometer.

When analyzing data, we need to specify energy scale. XPS analyzer measure the kinetic energy of the electrons. But XPS systems can have different x-ray sources so incident x-ray energy is not the same. Therefore, it is not wise to compare kinetic energy of the electrons because it will change with the energy of the incident x-ray. Therefore, it is common practice to use binding energy of the emitted electrons which is unique to the elements being tested.

One important factor that needs to be remembered is the spin-orbit splitting. Spin orbit coupling causes splitting of the binding energy peaks for electron orbitals other than the s orbital. Spin-orbit coupling occurs when the electron shell is partially full due to the unstable nature of the configuration. However, the spin and orbital momentum couple together to arrange the electrons into stable states. For each orbital shell p d and f there are two stable configurations; one for a shell that is more than half full and one for a shell that is less than half full. Table 1 documents the orbital and the common spin-orbital coupling configurations.

Table: 1 Spin-Orbital coupling configuration

Orbital	< Half Fill	>Half Fill
p	1/2	3/2
d	3/2	5/2
f	5/2	7/2

Different element has different split in the binding energy peaks but for a given element it is constant. This means that if the there is an energy shift due to electronegativity the difference between the split orbital peaks will remain the same.

Also, for the split orbital peaks the configuration with the highest coupled momentum will have the lowest binding energy. When the orbital is more than half fill the coupled momentum will be greater than the momentum of an orbital that is less than half fill.

Finally, the most important thing of the XPS is determine the chemical composition of the sample. This can be done from the electron binding energy peaks. The area under the binding energy curve is proportional to the number of atoms that emit the electrons at that binding energy. Therefore, if we take the ratio of the area under the binding energy curve for each element we can determine the composition of the samples surface. However, a sensitivity factor must be introduced for each element in this ratio. All XPS systems have different sensitivity factors making it difficult to obtain a precise composition without knowing the exact sensitivity factors. Following image shows (see figure 2.6) the main components of the XPS which we have in our laboratory.

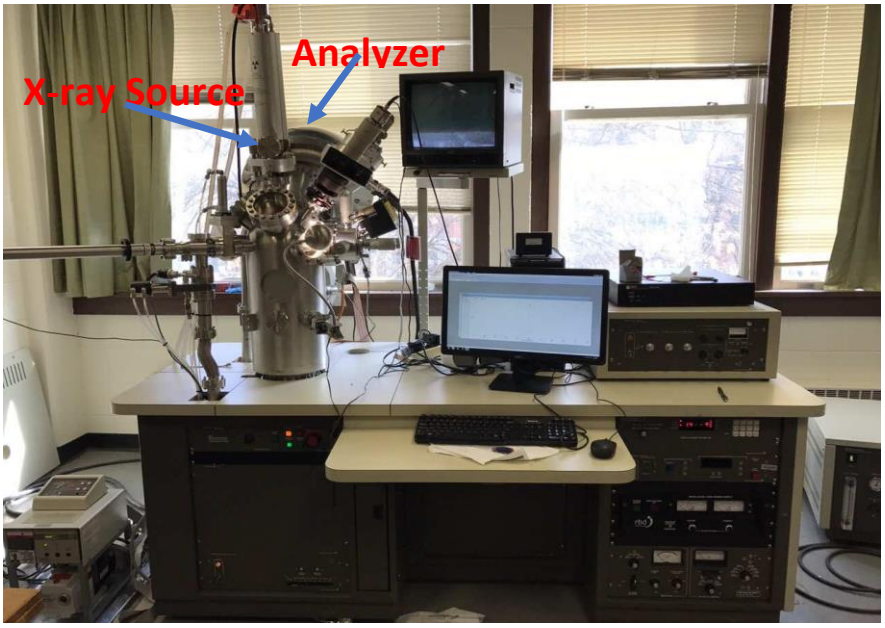

Figure 2.6 Main components of XPS

2.5: Transmission Electron Microscopy (TEM)

The TEM has the ability to determine the atomic positions inside a crystal lattice. Therefore, TEM is widely used in nanophysics and nanotechnology research and development in many fields such as semiconductor devices for photonics and electronic. There are mainly four parts of TEM electron source electromagnetic lens system sample holder and the imaging system.

Working principle of the transmission electron microscopy (TEM) is similar to optical microscopy but the difference is TEM is used electrons beams instead of photons in optical microscopy to form images of the sample being tested. Since the wave length of electrons are much smaller than the visible light TEM can achieved greater resolving power than the optical microscope. Usual resolving power of electron microscope is around 0.2 nm and magnification up to 2×10^6.

In TEM a tungsten (W) filament which is located at the top of the cylindrical column (Figure 2.7) is used to produce electron beams to illuminate the sample. The whole system is enclosed in vacuum with pressure around 10^{-4} Pa. Air and the other particles should be pumped out from the column to avoid collision of air molecules with electrons to avoid scattering of electrons.

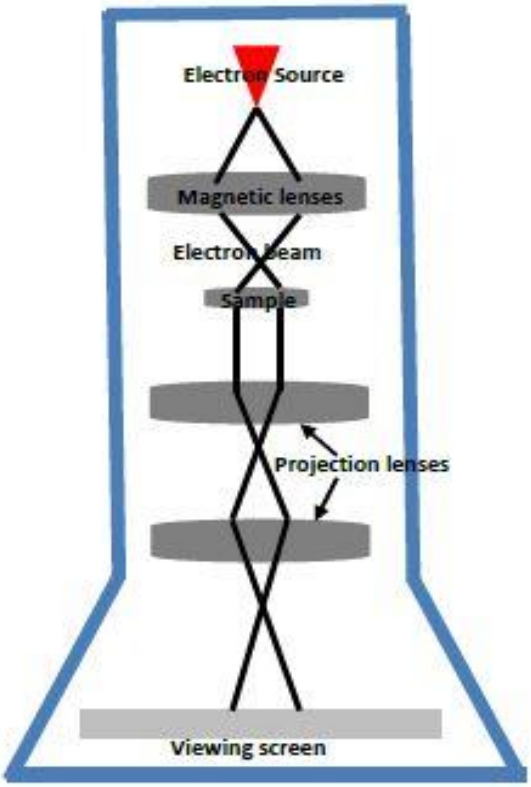

Figure 2.7 Schematic diagram of TEM

Along the long cylindrical type column at certain locations magnetic coils are placed to focus the electron beam. These magnetic coils act as electromagnetic condenser lens system. The sample stained with an electron dense material and is placed in the vacuum. Electron beams passes through the sample and scattered by the internal structures.

Electrons emitted by the heated filament in the electron gun travel towards the anode which is at positive voltage. Electrons travelling speed can be increased by increasing anode voltage. Faster the electrons move the smaller de Broglie wavelength they attain ($\lambda=h/mv$).

λ is de Broglie wavelength h is plank's constant m is electronic mass and v is speed of electrons. The resolution power is related with the wave length of the travelling electrons so shorter the wave length higher the resolving power. Therefore, the resolution of the TEM is increased if the accelerating voltage of the electron beam is increased.

The beam of electron that has been partially transmitted through the very thin sample carries information about the structure of the sample. The spatial variation in this information (the "image") is then magnified by a series of magnetic lenses until it is recorded by hitting a fluorescent screen photographic plate or light sensitive sensor like CCD (charge-coupled device) camera. The image detected by the CCD may be displayed in real time on a monitor or computer.

Figure 2.8 Main components of TEM

CHAPTER III

IRIDIUM SILICIDE NANOWIRES ON SILICON (110) SURFACE

3.1: Introduction

We studied physical and electronic properties of iridium silicide nanowires grown on the Si (110) surface with the help of scanning tunneling microscopy and spectroscopy. The nanowires grow along the [001] direction with an average length of about 100 nm. They have a band gap of ~ 0.5 eV and their electronic properties show similarities with the iridium silicide ring clusters formed on Ir modified Si (111) surface.

Ir (Iridium)-silicides have the lowest (highest) Schottky barrier for holes (electrons) which can be used in various device applications on silicon. For example, among silicides Pt (Platinum)-silicide/p-doped Silicon (Si) diodes are employed in large focal plane arrays for detection in the medium-wavelength infrared light (3–5 μm)[24]. The Schottky barrier height between Pt-silicide and p-doped Si (001) is about 0.23 eV corresponding to a cutoff wavelength of 5.4 μm [25]. In order to extend the cutoff wavelength, it is necessary to choose interfaces with lower Schottky barrier height. The Schottky barrier height between Ir-silicide/p-doped silicon is approximately 0.17 eV corresponding to a cutoff wavelength of 7 μm which makes Ir-silicide a promising material for infrared detector applications [26].

As continuous miniaturization challenges lithography techniques in electronics self-assembly based processes become more attractive. One particularly important self-assembled component is metal silicide nanowires. These nanowires can function as low resistance interconnects as fins in FinFET[27] devices and as nano-electrodes for attaching small electronic components within an integrated circuit. It has already been shown that a variety of metals form self-assembled silicide nanowires on the surface of flat and/or vicinal Si substrates [28 - 32]. Nanowires can be made up of various elements ranging from Bi [33] and rare-earth metals [34-36] to transition metals [37,38]. In comparison to Si (111) and Si (001) surfaces Si (110) surface has received relatively less attention because the surface reconstruction is complicated, and it is difficult to grow single large domains. However higher hole mobility in devices fabricated on Si (110) surface and the possibility of employing self-assembled nanowires in various applications have recently increased number of studies on these systems [39 -41]. Unlike 4-fold symmetric Si (001) surface Si (110) surface is two-fold symmetric which can lead to formation of nanowires along the same direction. Various studies have already reported the existence of metal silicide nanowires on Si (110) [42-47]. In this chapter we explain the formation of Ir-silicide nanowires and how growth temperature coverage and annealing time effect on the nanowires.

3.2: Experimental and Methods

The Si (110) samples used in the Scanning Tunneling Microscopy/Spectroscopy (STM/STS) experiments were cut from nominally flat 76.2 mm by 0.38 mm single side polished n-type (phosphorous doped R=1.0-10.0 Ohm-cm) wafers. The samples were mounted on molybdenum holders and contact of the samples to any other metal during preparation and experiment was carefully avoided. The STM/STS studies have been performed by using an ultra-high vacuum system (UHV) with a base pressure of 2×10^{-10} mbar equipped with an Omicron Variable Temperature STM. Before introducing Si (110) samples into the UHV chamber samples were washed with isopropanol and dried under the flow of nitrogen gas. Si (110) samples were degassed extensively and after that flash-annealed at 1250 °C. Then the samples were annealed at various temperatures to obtain various reconstructions of pristine Si (110) and Ir-silicide nanowires. (See details below) The sample temperature was measured with a pyrometer. The quality of the clean Si (110) samples was confirmed with STM prior to Ir deposition. Ir was deposited over the clean Si (110) surface from a current heated Ir wire (99.9 %). All the STM experiments were performed at room temperature. I-V curves measured while measuring high resolution STM images of the surface. Then the measured I-V curves were averaged. The local density of states curves (LDOS) were calculated out of the I-V curves [48].

3.3: Results and Discussion

Figure 3.1a and 3.1b show two STM images of pristine Si (110) surface before Ir deposition. It has been shown that the reconstruction of Si (110) surface depends strongly on the annealing temperature [49]. Annealing the sample at 600 ^{0}C leads to the formation of well-defined "16×2" domains however annealing at and above 800 ^{0}C disordered phase forms. (see Figure 3.1a and 3.1b) So far different structures have been proposed to explain Si (110) "16×2" structure [50-52]. The ad-atom-tetramer-interstitial (ATI) is the most accepted of them[53,54]. According to this model four ad-atoms of the top layer and one first layer atom come together and form a pentagon that surrounds an interstitial atom at its center.

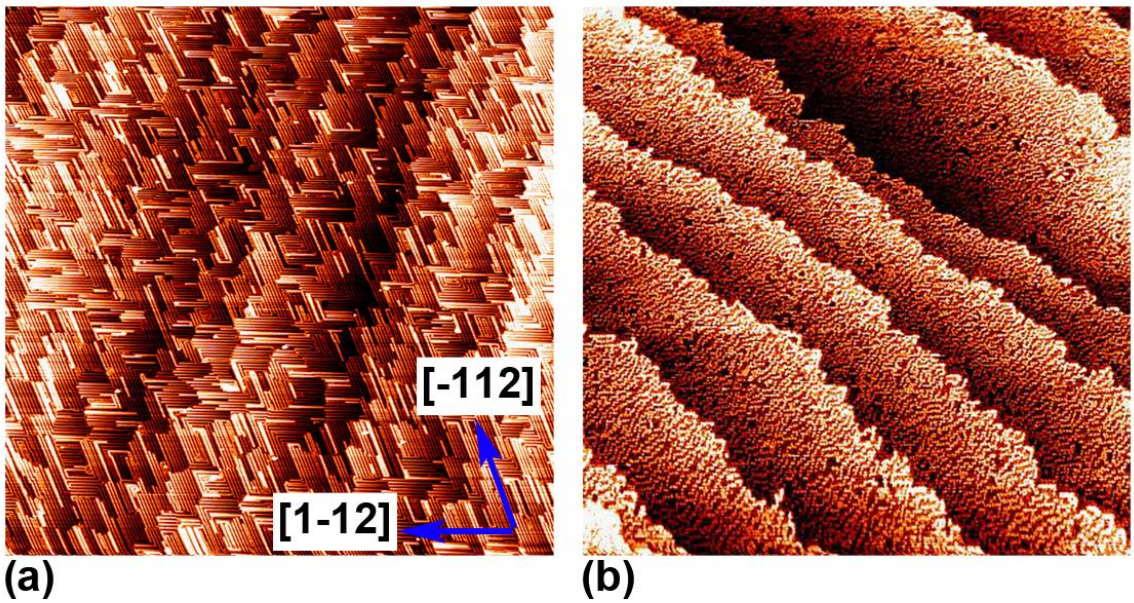

Figure 3.1 a and b are the STM images of clean Si (110) annealed at 600 °C and 800 °C respectively. The arrows indicate the high symmetry directions of the "16×2" domains. The sample bias and the tunneling current for the STM image in a (b) are -1.2 V (-1 V) and 0.2 nA (0.2 nA).

After depositing 0.25 ML of Ir on the surface the sample was annealed at 800 ^{0}C for two minutes while keeping the pressure below 2 × 10^{-10} mbar. Figure 3.2a shows a large scale STM image of the surface where several nanowires are visible. The nanowires grow along the [001] direction. Figure 3.2d shows a line scan graph measured on the nanowire shown in Figure 3.2b. The average height length and width of nanowires are 1.76 nm ± 0.32 nm 106.27 nm ± 21.76 nm and 14.63 nm ± 2.97 nm respectively. The variances in length and width are correlated since the values closely follow the equation

$$\sigma_A^2 = \langle W \rangle^2 \sigma_L^2 + \langle L \rangle^2 \sigma_W^2 + 2\langle W \cdot L \rangle \, \sigma_{LW} \tag{9}$$

Where $\sigma_A \, \sigma_L \, \sigma_W$ are standard deviations of the area the length and the width of the nanowires. $\langle W \rangle \, \langle L \rangle$ stand for expectation value of the width and the length of the nanowires. represent covariance of the width and the length of the nanowires. The strong correlation between the width and the length of a nanowire indicates that the length and the width must be physically coupled via strain diffusion and etc.

High resolution STM images similar to Figure 3.2b show that the terraces on which nanowires form have a superstructure that looks rather different than the pristine Si (110) surface. The superstructure has two equivalent domains that are rotated with respect to each other. (See Figure 3.3) Empty state image of the same region does not show any clear periodic structure.

(Figure 3.2c) With the help of the matrix notation the unit cell of the superstructure can be defined as (for domain A see Figure 3.3)

$$M_{terrace} = \begin{pmatrix} -4 & -1 \\ -2 & 3 \end{pmatrix}$$

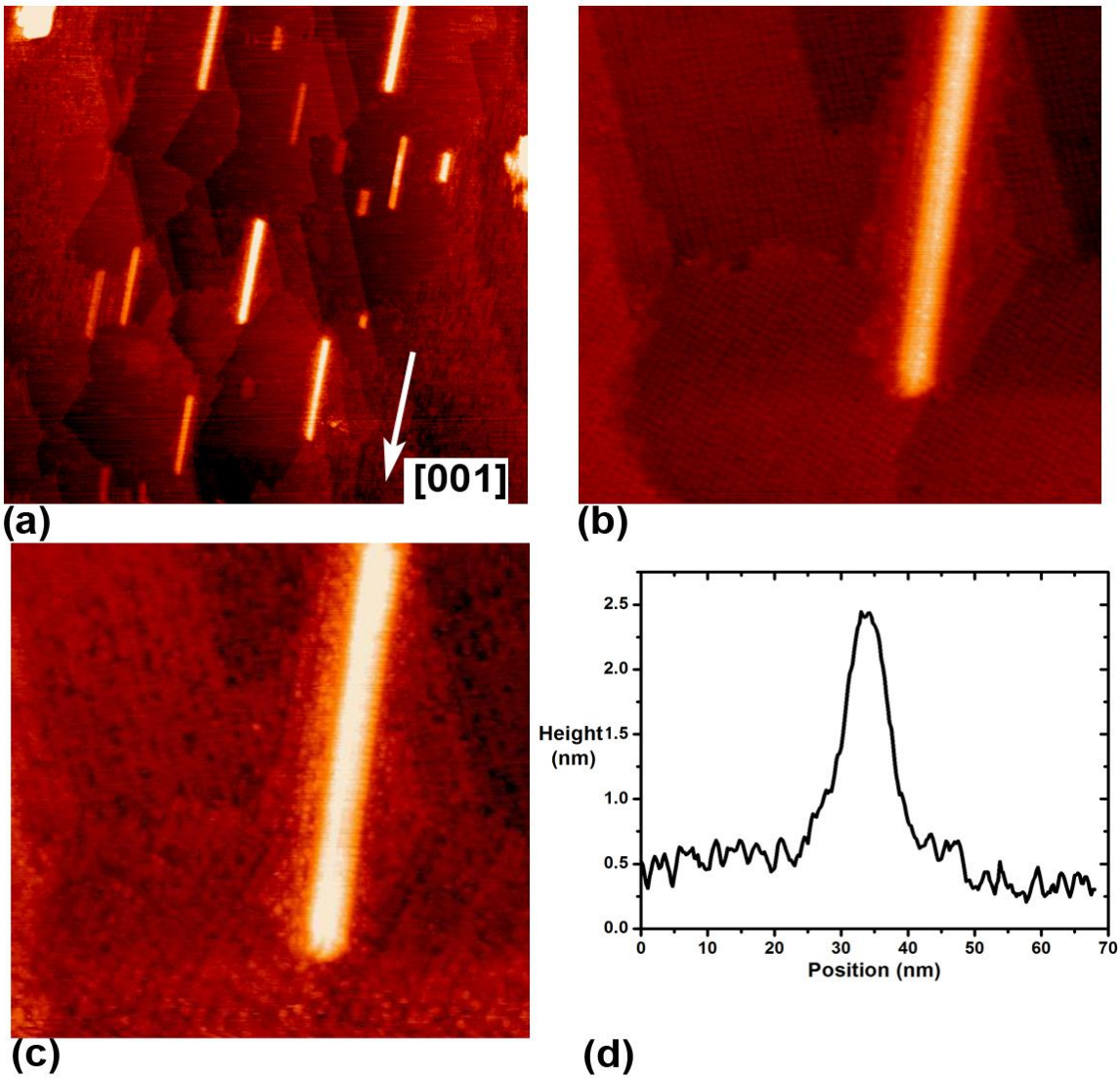

Figure 3.2 (a) is a 400 nm × 400 nm and (b) is a 100 nm × 100 nm STM images of Ir modified Si (110) surface. Ir silicide nanowires grow along [001] direction

A careful analysis of STM images revealed that there are domain walls even within a single domain of the superstructure. (See Figure 3.3) These walls separate well defined periodic regions marked by the green rectangles. The domain walls are even thicker than the domains themselves indicating that the corrugation of the superstructure/substrate potential is significantly small compared to the lateral interactions between the constituents of this superstructure [55].

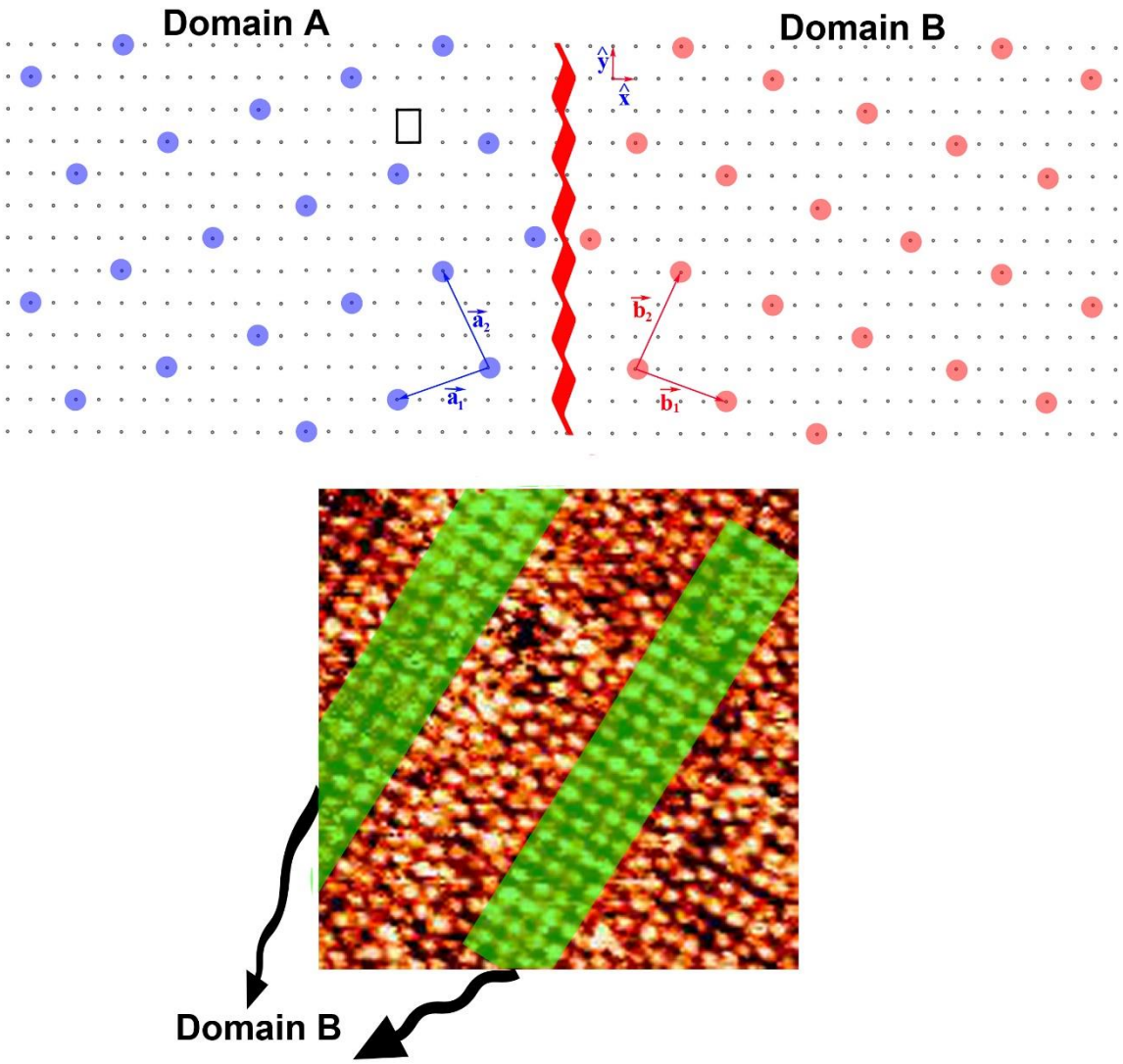

Figure 3.3 Top A schematic diagram of domain A (left) and domain B (right) of the superstructure is presented. $\hat{x}$ and $\hat{y}$ are basis vectors of Si (110) lattice pointing along [1-10] and [001] directions. Bottom: An STM image of the terrace showing the two B-type domains (green rectangles) separated by a domain wall

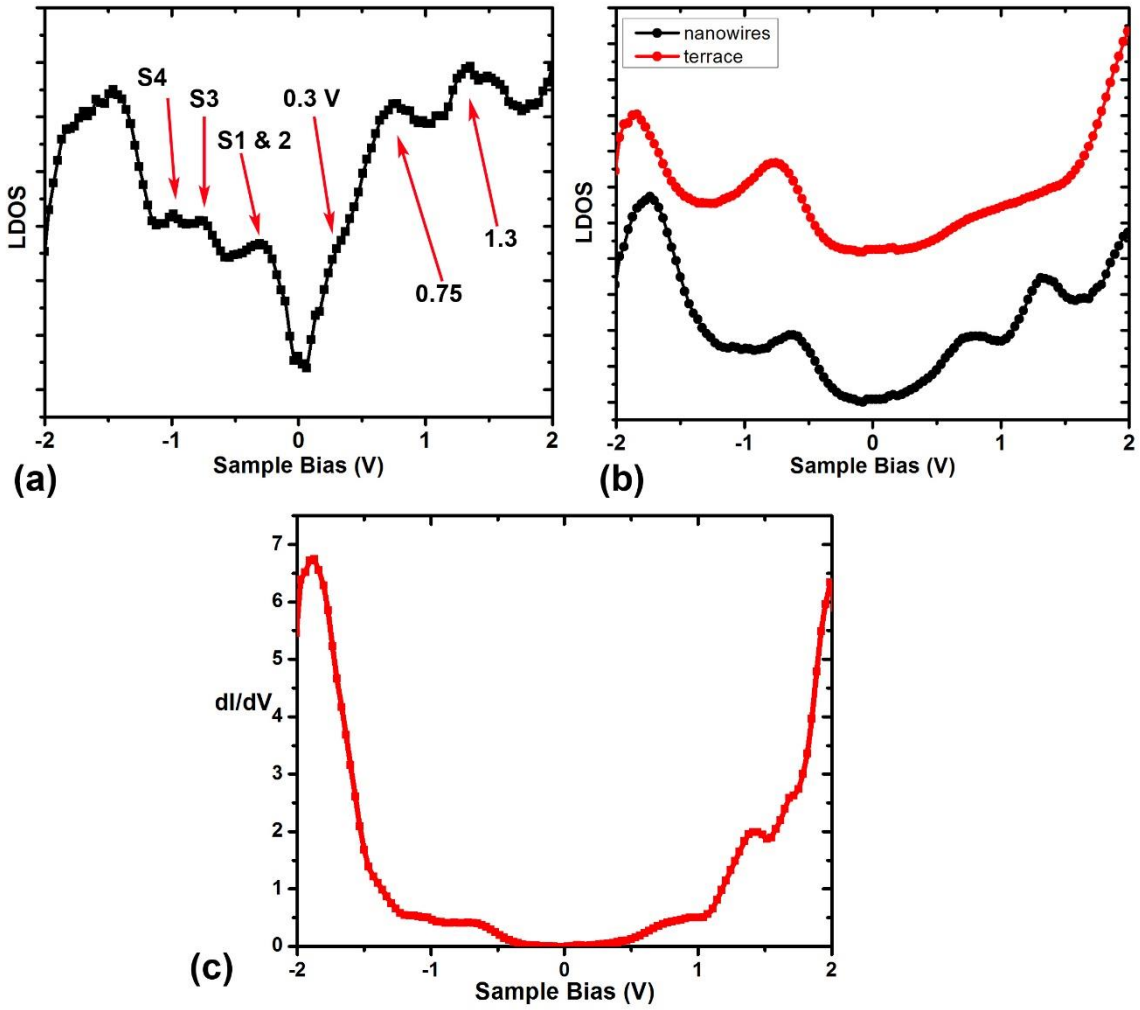

Figure 3.4 (a) LDOS graph measured on pristine Si (110) "16 × 2" surface. (b) LDOS graphs measured on Ir-silicide nanowires (black) and terrace surrounding the nanowires (red). (c) dI/dV graph measured on Ir-silicide nanowires that shows a gap of about 0.5 eV.

Kim et. al. studied the electronic structure of Si (110) “16 × 2” surface with angle resolved photoemission spectroscopy (ARPES) [56]. Their data show that there are four surface states located at -0.2 eV (S1) -0.4 eV (S2) -0.75 eV (S3) and -1.0 eV (S4). Later with the help of STS measurements the state at -0.2 eV was assigned to the pentagons and the rest of the states were attributed to the surface states at the step edges [57].

Figure 3.4a shows the LDOS curve we measured. The LDOS curve reproduced most of the states below the Fermi level. One important difference is that the LDOS curve has a just single peak located at -0.3 eV instead of two peaks at -0.2 eV and -0.4 eV as measured with ARPES. This can be due to the broadening of the STS peaks. The broadening corresponds to approximately 0.1 eV at room temperature [57]. LDOS data published by Setvín et. al. also shows a single peak albeit their peak is located at 0.2 eV [58]. On the other hand, the LDOS graph has a shoulder at 0.3 eV and two well resolved peaks at 0.75 eV and 1.3 eV which are also attributed to pentagons on the surface.

Figure 3.4b shows two LDOS curves measured on Ir-silicide nanowires (black) and the terrace (red) surrounding them. The nanowires and the terrace have band gap of about 0.5 V (see Figure 3.4c) which is significantly wider than the band gap of “16 × 2” domains (~ 0.2 eV). Both LDOS curves have one well-resolved peak below the Fermi level. The peak coincides well with a well-known projected bulk band. However, it can still have some surface contribution. Previously we studied Ir ring clusters on Si (111) surface extensively [59,60]. Ab-initio density functional theory calculations performed on this surface revealed that

below the Fermi level there is a state associated with Ir atoms embedded in the ring clusters. The position of this state in the spectrum almost perfectly matches with the peaks observed on the Ir-silicide nanowires and the underlying terrace. Above the Fermi level the LDOS curves in Figure 3.4b look different. The terrace has a broader feature originating from conduction band. On the other hand, the nanowires have two well-resolved states located at 0.75 eV and 1.4 eV. The position of these peaks are comparable to the position of peaks measured on Ir ring clusters. On Ir ring clusters we determined that these peaks belong to Ir atom and six Si adatoms that constitute the rings. Similarities on the electronic properties between the two surfaces suggest that the building blocks of these nanowires may resemble Ir-ring clusters.

3.4 Conclusions

In summary we report the formation of Ir – silicide nanowires on Si (110) surface. The average length of a nanowire is about 100 nm. Statistical analysis of the size distribution reveals that the length and the width of the nanowires are correlated. This provides an opportunity to adjust the dimensions of these nanowires by changing growth parameters for the specific application. Ir– silicide nanowires are semiconductor with a band gap of about 0.5 eV. The position of the electronic states is similar to the Ir-ring cluster of Ir modified Si (111) surface. Although we could not obtain a ST M image that shows internal structure of the makings of the nanowires and the underlying superlattice the similarities of the

electronic properties between Ir–silicide nanowires and Ir-ring clusters suggest that the chemical composition of both surfaces may be similar.

CHAPTER IV

COULOMB BLOCKADE AND NEGATIVE DIFFERENTIAL RESISTANCE AT ROOM TEMPERATURE:

SELF ASSEMBLED IRIDIUM QUANTUM DOTS ON SILICON (110) SURFACE

4.1 Introduction

We recently showed that Ir-silicide nanowires would grow on Si (110) surface after depositing a quarter of a monolayer of Ir and annealing the sample at 800 °C. The nanowires grow along [001] direction and have a band gap of about 0.5 eV .[61] However, when the amount of Ir coverage on the surface is increased to two monolayers large relatively flat terraces start to grow. A closer look at these terraces reveals that these terraces are not atomically flat but corrugated with quasi-periodic metallic Quantum Dots (QDs). It has been known that by controlling the deposition and annealing temperatures small islands of different sizes and symmetries can form on closely packed surfaces of noble metals.[62] For example, during epitaxial growth on Ag (111) surface at room temperature Ag atoms form islands that are one-atom thick. [63,64] Another example is the growth of the second layer of Na atoms on Cu (111) surface grows via island formation.[65-67] The final morphology of the surface depends strongly on the interaction of adatoms with the substrate as well as parameters of the growth process such as evaporation rates, temperature, pressure, and etc.[68-70]

By designing surfaces with a certain strain-relief pattern, it is possible to form ordered arrays of equally spaced monodispersed quantum dots by atom diffusion and deposition.[71] Therefore, observed quasi periodic lattice of Ir-QDs suggests that on this surface there must be a certain strain-relief process which limits adatom diffusion along certain direction and limits the size of QDs' reaching beyond certain limit.

In general, QDs can be metallic or semiconductor. In a semiconductor QD electrons are confined in all three dimensions down to a length scale in the order of Fermi wavelength therefore the energy spectrum of a QD becomes discrete. Because of that the semiconductor QDs may also be called as artificial atoms. In metallic QDs the electrons have relatively high density large effective mass and short phase coherence length which magnifies the importance of the charging energy associated with Single Electron Tunneling (SET) to/from the QDs while downplaying the quantized energy spectrum. In a large metal island charging effects due to the transfer of a single electron across a junction is negligible and usually associated with shot noise.[72] However for sufficiently small islands charging starts to play a significant role in the tunneling spectrum.[73-77] An activation energy is required to overcome the electrostatic force between electron tunneling to/from the island and the charge of the island.[78] Due to this activation energy it is not possible to pass current when the bias across the tunnel junction is lower than certain threshold value. In analogy with the opening of a band gap of a semiconductor this reduction in the conductivity around zero bias is called Coulomb blockade. To observe Coulomb blockade the total capacitance of the QDs should be smaller than $e^2/2kT$ and the resistances of the tunnel junctions should be larger than the resistance quantum $h/2e^2$. [79]

In this chapter we report Scanning Tunneling Microscopy/Spectroscopy (STM/STS) data to reveal structure and electronic properties of Ir-QDs which exhibit both Coulomb blockade and negative differential resistance at room temperature. We also present X-ray Photoelectron Spectroscopy (XPS) data to discuss chemical composition of the surface.

4.2 Experimental and Methods

The Si (110) samples used in this paper were cut from nominally flat 50.8 mm × 0.5 mm double side-polished n-type (phosphorous doped R=0.05-0.5 Ohm-cm) wafers. The samples were mounted on Mo holders and contact of the samples to any other metal during preparation and experiment was carefully avoided. The STM/STS studies have been performed by using an ultra-high vacuum system (UHV) with a base pressure of $2 \times 10^{-10}\ mbar$. The XPS experiments were conducted in a PHI-5400 XPS system with a base pressure of $2 \times 10^{-10}\ mbar$. The XPS system also has Ar^{+} ion sputter gun. Before introducing Si (110) samples into the UHV chamber samples were washed with isopropanol and dried under the flow of nitrogen gas. Si (110) samples were degassed extensively and after that flash-annealed at 1250 °C. Sample temperature was measured with a pyrometer. The quality of the clean Si (110) samples was confirmed with STM prior to Ir deposition. Ir was deposited over the clean Si (110) surface from a current heated Ir wire (99.9 %). All the STM experiments were performed at room temperature. I(V) curves measured at every point of the image while measuring an STM images of the surface.

Then the measured I(V) curves were averaged. The dI/dV curves were calculated from the measured I(V) curves.[80] Once the samples were prepared in the STM chamber they were quickly transferred to the XPS chamber with 2×10^{-10} mbar base pressure. The samples were sputtered for 8 mins with 1 KeV Ar^+ ions. The samples were measured by an Al Kα (1486.6 eV) X-ray source with a pass energy of 89.5 eV (1 eV/step) and 8.95 eV (0.025 eV/step) for survey and high-resolution scans respectively. We analyzed all the XPS core-level spectra with least-squares minimization curve fitting program. Si (Ir) core-level peak was fitted using a symmetric (asymmetric) Gaussian instrument response function convolved with Lorentzian core-level line shape (GL).

For both Ir 4f and Si 2p peaks the secondary electron background was subtracted using a Shirley function.[81]

4.3 Result and Discussion

Figure 4.1a shows a 0.52 µm × 0.52 µm STM image of the Ir modified Si (110) surface after depositing two monolayers of Ir on atomically clean Si (110) surface and subsequently annealing the sample at 800 °C for 2 minutes. As shown in Figure 4.1a and 4.1b the surface was partially covered with flat terraces. The high symmetry directions of the underlying Si (110) surface are shown by green and blue arrows in Figure 4.1. Figure 4.1b is a 57 nm × 57 nm image of the surface showing that the terraces are not actually atomically flat but covered with QDs. Si surface visible through the gaps between the islands do not exhibit an

ordered structure. Figure 4.1c is a higher resolution STM image measured on one of these terraces. The QDs on the islands form a quasi-periodic structure on the surface. The average distance between the QDs was calculated by taking the fast Fourier transform of the measured line scans across the surface. (not shown) The average distance between QDs was about 1.53 nm along [001] direction and 1.0 nm along [1-10] direction. The average diameter of QDs was about 0.8±0.2 nm. We tried measuring STM images at various sample bias/tunneling current combinations however it was possible to obtain decent images only when high voltage/low tunneling current setting were used. This setting translates into larger tip/sample separations. We attributed unstable tunneling conditions for smaller tip/sample separation to the fact that QD's were loosely attached to the surface and the electric field between the tip and sample was strong enough to move them around.

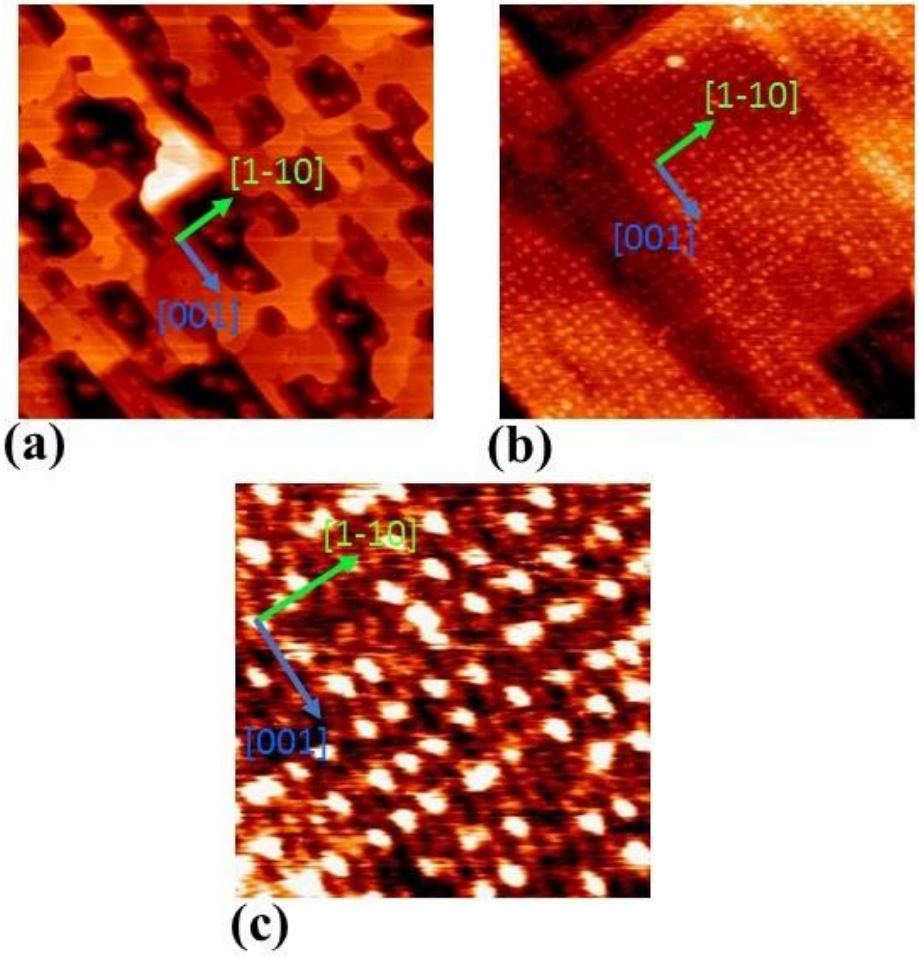

Figure 4.1 (a) is 0.52 µm × 0.52 µm STM image tunneling voltage/current are -1.48 V and 0.47 nA (b) 57 nm × 57 nm STM image tunneling voltage/current are -1.97 V and 0.30 nA and (c) 13 nm × 13 nm STM image tunneling voltage/current are -1.93 V and 0.24 nA. The green and blue arrows indicate high symmetry directions of the underlying Si (110) surface

To study electronic properties of the surface we measured the I(V) curves (Figure 4.2) on both the QD's and the terrace and then calculated the dI/dV curves. The dI/dV curves measured on the terrace show non-zero conductance indicating metallic nature of the terraces. On the other hand, the dI/dV curves measured on the QD's has suppressed conductance around the Fermi level. Suppressed conductance around the Fermi level is a well-known signature of Coulomb blockade.

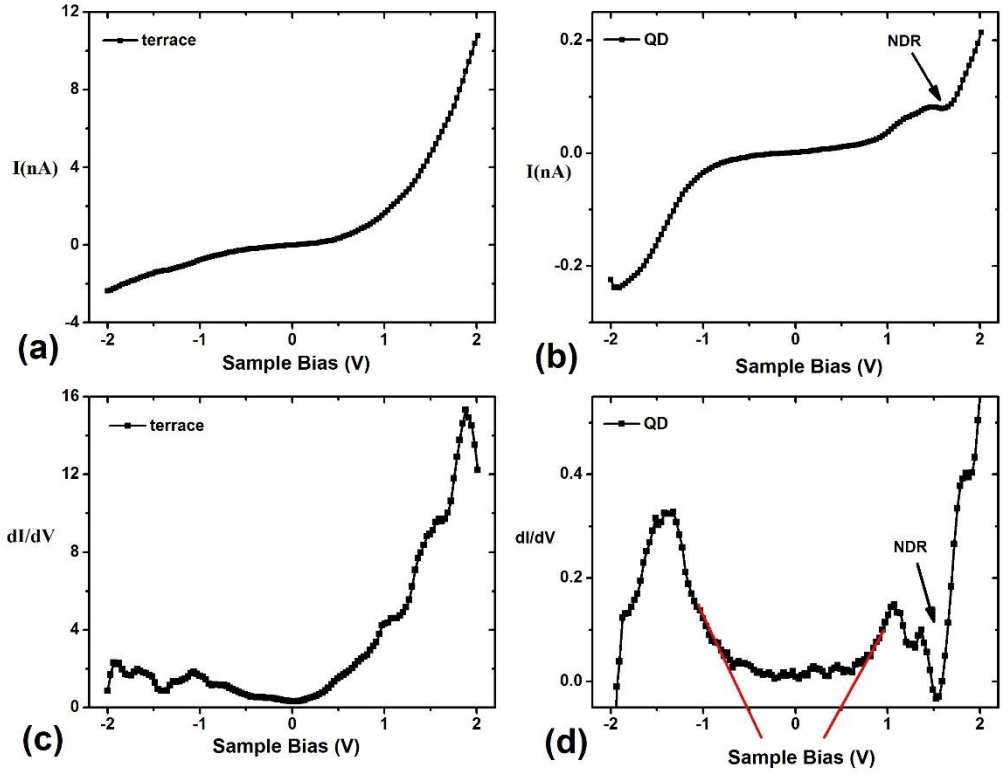

Figure 4.2 (a) and (b) are I(V) curves measured on terrace and on a QD respectively. (c) and (d) are dI/dV curves numerically calculated from the I(V) curves in (a) and (b). In (b) and (d) NDR is indicated with an arrow. Red lines in (d) is to guide the eye for Coulomb gap.

Experimental I(V) curve is almost linear characteristic of ohmic behavior between -1 V to 1 V which allows us to use orthodox theory of single electron tunneling.[82] According to this theory the system at hand can be considered as two tunnel junctions connected in series. The first tunnel junction is located in between the STM tip and the QD and the second tunnel junction is between the QD and the substrate. Each tunnel junction leaks slowly via tunneling. QDs are directly on top of the terraces with no insulating layer in between which suggests strong coupling and low resistance. However, to observe Coulomb gap the tunneling resistance of each tunnel junction must be high enough ($R \gg \frac{h}{e^2} \cong 26\ k\Omega$) to trap charges in the QD for long enough to create Coulomb repulsion for the incoming electrons. Another important point to note is the absence of Coulomb staircase indicating that the resistance and capacitance of the tunnel junctions are approximately the same. By using orthodox theory of single electron tunneling as described in reference 82. we calculated I(V) curves to predict the total resistance capacitance of the tunnel junctions and the fractional charge on the QD's. The equivalent resistance and capacitance of the circuit are $2 \times 10^{10}\Omega\ 5 \times 10^{-19}F$ respectively. Because of the fractional charge on the QD I(V) curve has non-zero slope around the Fermi level. I(V) curve calculated for a fractional charge of 0.5e (Figure 4.3) is the best to represent the experimental data. While keeping resistance and capacitance of the double junction the same and reducing the fractional charge on the QD to zero makes the slope of the I(V) curve zero around the Fermi level.

Another important feature on the experimental dI/dV curve is the presence of Negative Differential Resistance (NDR) measured at around 1.5 V. NDR is a decrease in the tunneling current with increasing voltage which has been observed on QDs and molecular electronics.

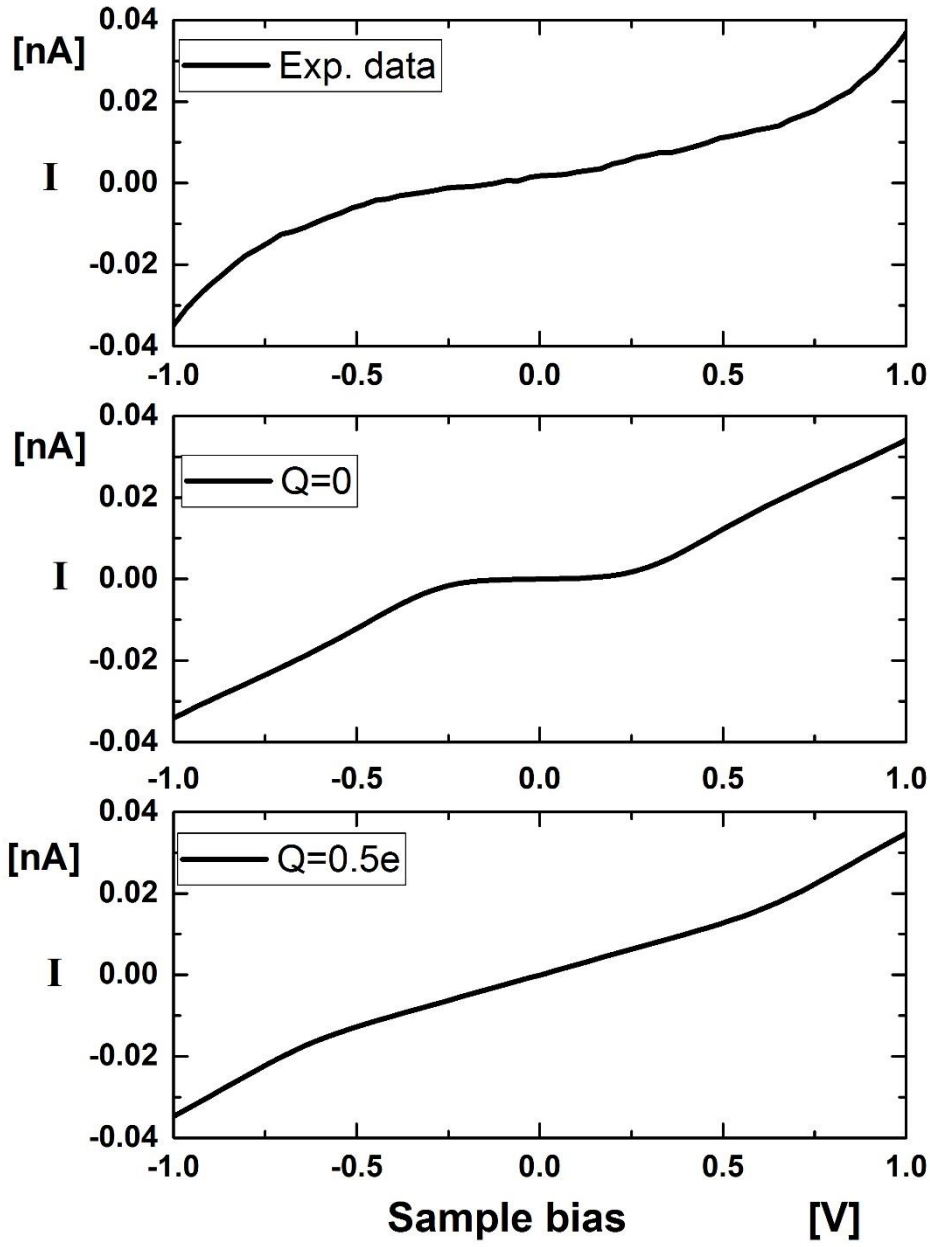

Figure 4.3 Top: Measured I(V) curve shown between -1 V to 1 V, Middle and bottom: Simulated I(V) curves with fractional charge 0 and 0.5e, respectively.

With STM/STS we studied the morphology of the surface and its electronic properties. However, STM/STS do not offer much information about the chemical properties of the surface. To study that we performed XPS measurements. On the pristine Si (110) sample the binding energy of the Si 2p peak was measured at 99.9 eV (Figure 4.4a) which is 0.6 eV above the bulk Si 2p peak reported in the literature.[83] The shift indicates that the surface defects created during sputtering pinned the surface Fermi level above the edge of the bulk valence band. To equilibrate the Fermi levels of the bulk and the surface the electrons from the bulk donor level was transferred to the empty surface states creating a depletion layer and band bending. On the other hand, the XPS data of Si 2p peak of QD sample had two peaks (Figure 4.4b). One of them was originating from the bulk Si atoms and it was located at 99.57 eV. In comparison to pristine Si (110) sample the Si 2p peak was shifted to a lower binding energy. This was expected when Si and a high work function metal (such as Ir) are in contact the surface Fermi level pins closer to the valence band edge of Si which reduces the band bending and shifts the binding energy of Si peaks to lower values. We attributed the second peak in XPS spectra of Si to the Ir-silicide formed at the interface. The binding energy of this peak was at 100.19 eV which indicates a chemical shift of 0.62 eV towards the higher binding energy. Table in Figure 4.5b summarizes Si 2p peak positions with the various bulk Ir-silicide compounds reported previously.[84-86] Among the known Ir-silicides the shift in Si 2p peak is closer to $IrSi_{1.6}$.

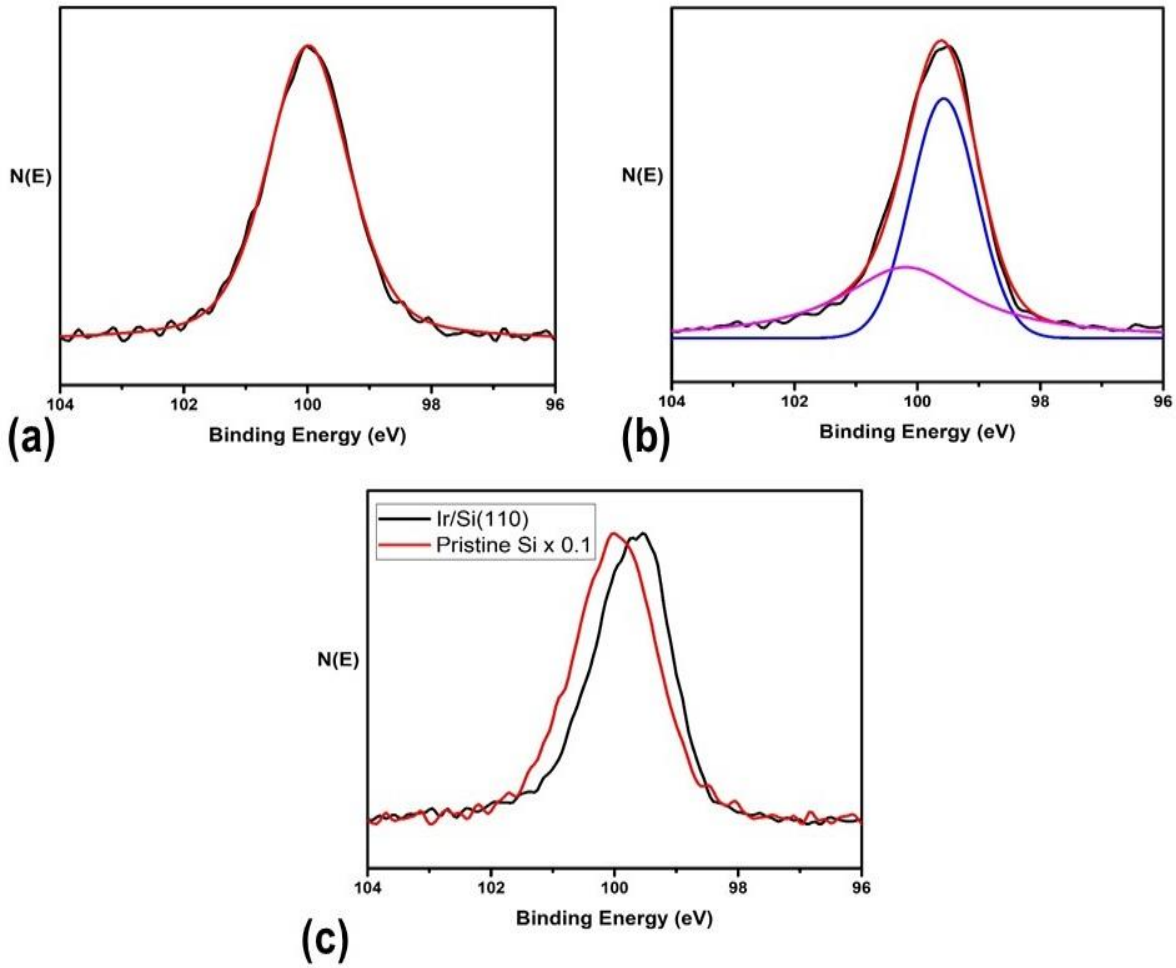

Figure 4.4 (a) and (b) show Si 2p peak measured on sputter cleaned Si (110) and QDs/Si (110) samples respectively. (c) Raw data measured on sputter cleaned Si (110) and QDs/Si (110)

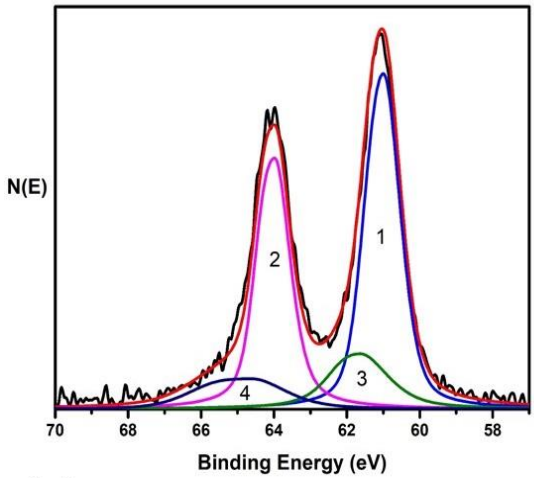

(a)

Compound	ΔE_B (eV)[1]	ΔE_B (eV)[2]	ΔE_B (eV)[3]	ΔE_B (eV)[4]
IrSi (Ir 4f)/(Si 2p)	-0.10/+0.30	0.00/+0.30	-0.20/+0.60	-
$IrSi_{1.6}$ (Ir 4f)/(Si 2p)	+0.50/+0.60	+0.30/+0.40	-	-
$IrSi_3$ (Ir 4f)/(Si 2p)	+0.55/+0.55	-	-	-
Ir QDs on Si(110) (Ir 4f)/(Si 2p)	-	-	-	+0.64/+0.62

(b)

Figure 4.5 (a) Ir 4f peaks measured on QDs/Si (110) sample. (b) Table summarizing shifts in Ir 4f and Si 2p peaks in various Ir-silicides. [1]Ref [23][2]Ref [24] [3]Ref [25] [4]This work.

Figure 4.5a shows Ir 4f peaks measured on a QD sample. The peak exhibits a clear spin-orbit splitting fitted with four GL peaks to represent the two doublets originating from Ir bulk and Ir-silicide. Both the energy difference and the area of the $4f_{5/2}$ peaks (peak 2 & 4) were fixed with respect to the $4f_{7/2}$ peaks (peak 1 & 3). The binding energy of the $4f_{5/2}$ peaks were set 2.98 eV higher than that of the $4f_{7/2}$ peaks and the area ratio between them were kept 3:4. The binding energy of bulk Ir $4f_{7/2}$ peak (1^{st} peak) was at 61 eV which is in line with the literature for pristine Ir suggesting that terraces are made out of Ir.[87] On the other the $4f_{7/2}$ peak (3^{rd} peak) associated with silicide formation was located at 61.69 eV. Although the shift in this Ir peak is relatively large compared to the shift measured in the bulk Ir-silicides a quick comparison of the position of Ir 4f peak in various bulk Ir-silicides reveal that the shift

gets larger as the Si content of the Ir-silicide gets higher as expected. In this study Ir was deposited on Si (110) surface and at the interface on average Ir atoms may be surrounded by more Si atoms than the reported bulk Ir-silicides causing a higher shift in the binding energy of Ir 4f peak.

4.4 Conclusions

We performed extensive STM/STS and XPS measurements on metallic QDs formed on Ir modified Si (110) surface. The QDs were weakly adsorbed on the surface and formed quasi periodic superstructure on the terraces. The dI/dV curves measured on QDs showed opening of a Coulomb gap around the Fermi level indicating that STM tip/QDs/terrace formed a double junction system. XPS data shows that at the interface between the Ir terraces and Si substrate silicide layer forms. Both Ir 4f and Si 2p peaks associated with the silicide shifted to higher binding energies. Out of known bulk Ir-silicides the shifts in Ir 4f and Si 2p peak were closer to Si-rich silicides i.e. $IrSi_{1.6}$ and/or $IrSi_3$.

CHAPTER V

CROSS SECTIONAL ANALYSIS OF IRIDIUM SILICIDE NANOWIRES ON SILICON (110) SURFACE

5.1 Introduction

At certain stage lithography-based techniques will not be able to meet the challenges faced by the electronics industry and we need to develop processes based on self-assembly. Self-assembled metal-silicide nanowires have the potential to play a key role in this transition. These nanowires can be used not only low-resistance interconnects but also fins in FinFET (Fin field effect transistors)[88] devices and as nano-electrodes for attaching small electronic components within an integrated circuit. A variety of self-assembled metal-silicide nanowires have been shown to form on the surface of flat and/or vicinal Si substrates.[89-93] Metals in these nanowires can range from Bi[94] and rare earth metals[95-97] to transition metals.[98,99] Although Si (110) has complicated surface reconstruction, higher hole mobility and growth of self-assembled nanowires have recently increased the number of studies on this surface.[100-102]

Unreconstructed Si (001) surface is four-fold symmetric. However unreconstructed Si (110) surface has two-fold symmetry leading to the formation of nanowires growing along the same direction.

The formation of metal-silicide nanowires on Si (110) have been reported before. [103-108] The formation of nanowires on Ir modified Si (110) have been discussed in the previous chapters however the presented STM data has limited information regarding the actual crystal structure of the nanowires. In order to reveal the true structure of these nanowires we measured High-Resolution Transmission Electron Microcopy (HR-TEM) of the cross section of the nanowires. Cross-sectional TEM images of the Ir-silicide nanowires were taken at the Oak Ridge National Laboratory (ORNL) in collaboration with Dr. Karren More. (see Figure 5.1) Nanowire samples were prepared at UND and thin slices of cross-sections of these samples were prepared at ORNL. TEM images were analyzed using ImageJ software.[103] To make the models of the crystals we used VESTA software.

5.2 Experimental and Methods

The Si (110) samples were cut from nominally flat 76.2 mm by 0.38 mm single side-polished n-type (phosphorous doped R=1.0-10.0 Ohm-cm) wafers. The samples were mounted on molybdenum holders and contact of the samples to any other metal during preparation and experiment was carefully avoided. The STM/STS studies have been performed by using an ultra-high vacuum system (UHV) with a base pressure of $2 \times 10^{-10}\ mbar$. Before introducing Si (110) samples into the UHV chamber samples were washed with isopropanol and dried under the flow of nitrogen gas. Si (110) samples were degassed extensively and after that flash-annealed at 1250 °C. The sample temperature was measured with a pyrometer. The quality of the clean Si (110) samples was confirmed with STM prior to Ir deposition. Ir was deposited over the clean Si (110) surface from a current heated Ir wire (99.9 %). All the STM experiments were performed at room temperature. I-V curves measured while measuring high resolution STM images of the surface. Then the measured I-V curves were averaged. The derivative of the I-V curves were calculated numerically.

5.3 Results and Discussion

Figure 5.1a shows high symmetry directions of Si (110) surface. By comparing high symmetry directions of pristine Si (110) surface with the nanowire directions we concluded that the nanowires grow parallel to [001] direction. Figure 5.2 shows TEM images of cross section of a nanowire. Ir-silicide nanowires grow into the substrate. This type of growth is called endotaxial growth. The term "endotaxy" refers to the growth of implanted species in a bulk matrix with interfaces coherently surrounding the new species.[104] Interesting and useful structures can be formed by endotaxy as in thermoelectric or magnetic systems.[105-106]

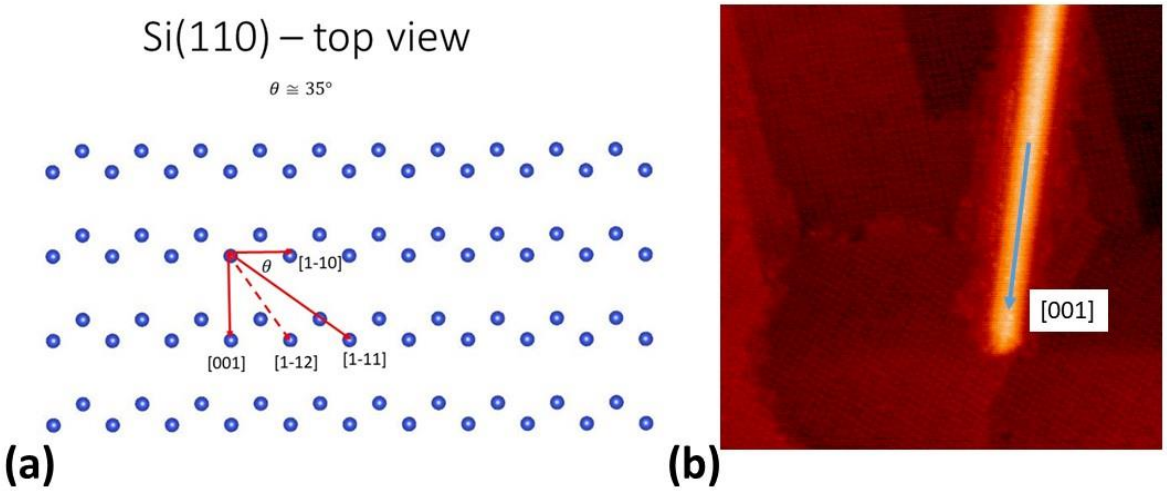

Figure 5.1 (a) a top view of the Si (110) surface with high symmetry directions. (b) an STM image of a Ir-silicide nanowire. The arrow indicates [001] direction.

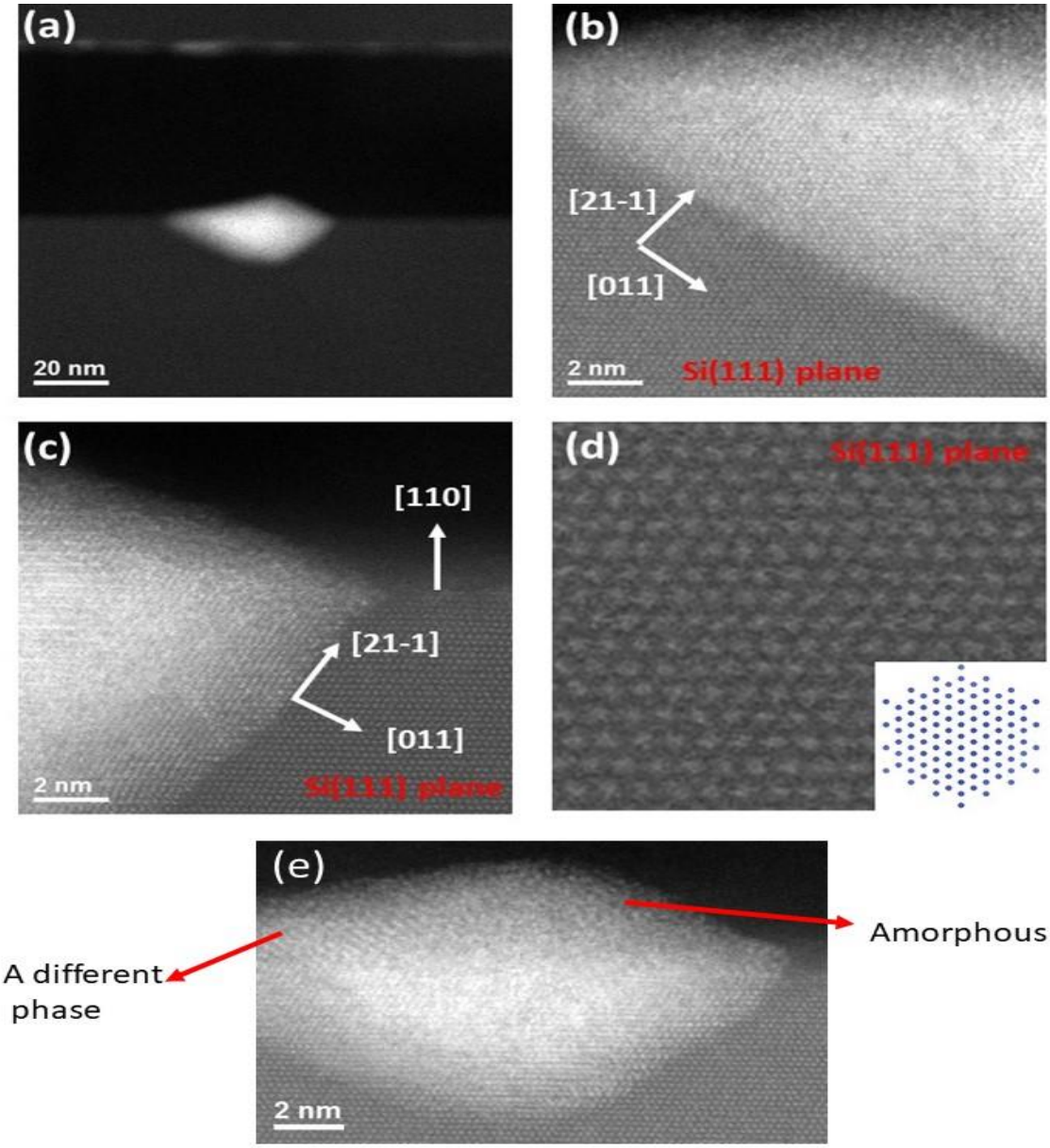

Figure 5.2 (a) shows a cross-sectional image of a NW grown under similar conditions. (b) and (c) are higher resolution images of the same NW. (d) shows a higher resolution image of the Si (111). Inset: is a model of the bulk Si oriented towards (111) direction. (e) Shows a cross-section of another nanowires top-left part of the nanowire has another phase and the rest of the top part looks amorphous.

By analyzing the distance between the crystal planes of the nanowires and comparing it with the known crystal phases of Ir-silicides we concluded that the nanowires are made out of $IrSi_2$. (see Figure 5.2a-c) $IrSi_2$ crystalizes in the cubic structure (space group Fm-3m a fluorite structure) with the lattice constant $a = 5.65\ \text{Å}$. (See Figure 5.3) $IrSi_2$ bulk is metallic.[107] Formation of $IrSi_2$ has been observed on Ir films grown on Si (001) surface but it has not been reported as one of the stable bulk phases.

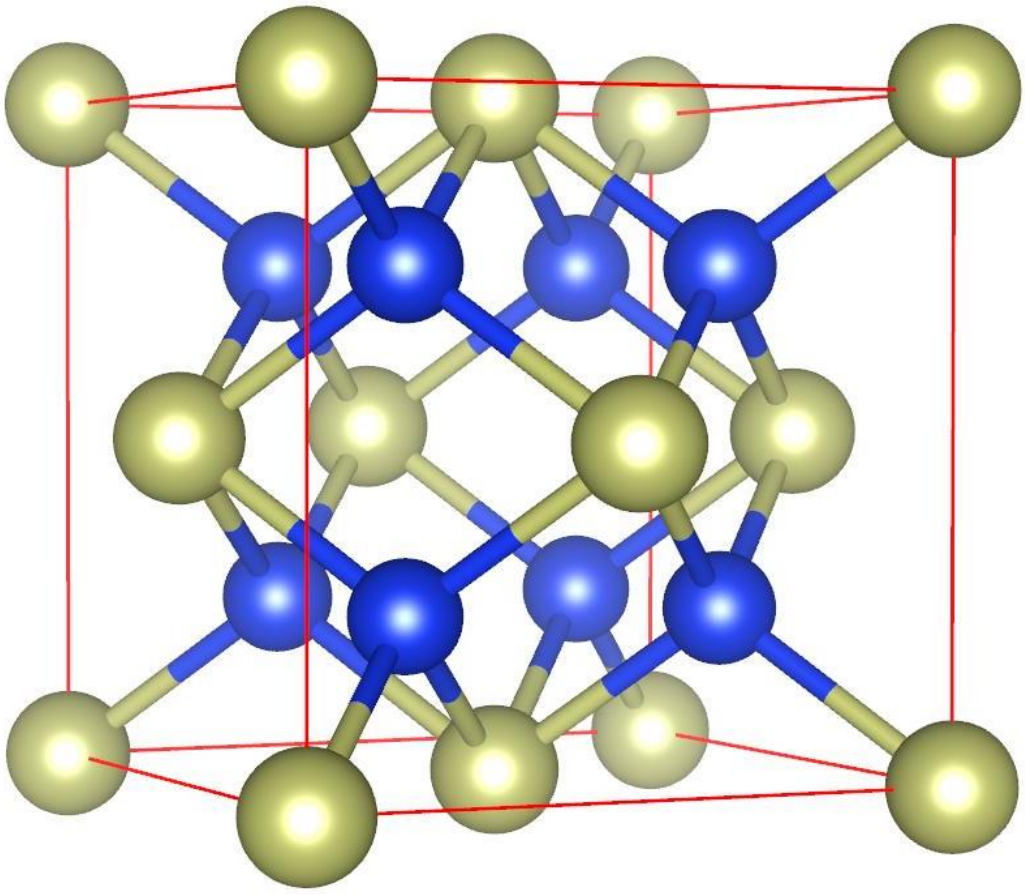

Figure 5.3 Bulk structure of fluorite-type $IrSi_2$. Blue/yellow atoms are Si/Ir.

Analysis of the TEM images of Si surface showed that the sample was cut perpendicular to the [111] direction of the Si crystal. (see Figure 5.2d) In other words the cuts we have is not perpendicular cross section of the nanowires instead there is an angle of approximately 55° between (111) and (001) planes of the nanowires. The measured facet orientations of nanowires are {21-1} and {011} directions respectively. In order to reveal true view of the nanowires when cut perpendicular to [001] direction we rotated both facets 55° around [110] direction and calculated orientation of the facets (see Figure 3a and 3b)

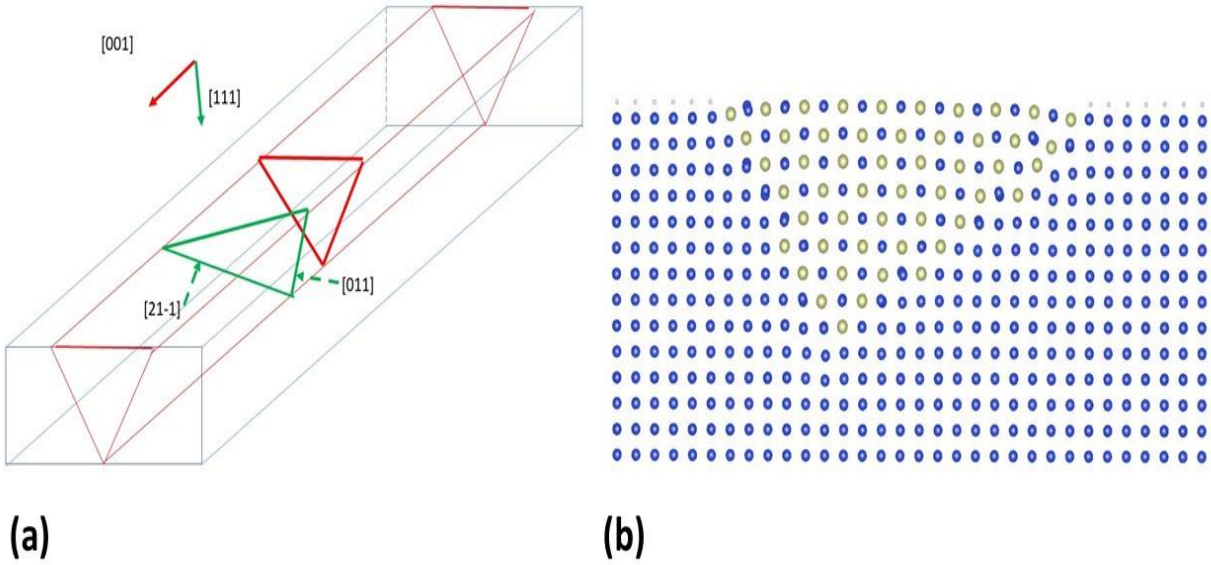

Figure 5.4 A schematic to show both cut direction on a hypothetical nanowire. Red triangle is on (001) plane and green triangle is on (111) plane. The two facets observed on the TEM images are indicated on the green triangle. (b) is an atomic model showing what we would have seen if the sample were cut along (001) direction.

dI/dV curves measured on nanowires with various widths showed a curious trend (see Figure 5.5). Although dI/dV curves show quite similar features above the Fermi level below the Fermi level valence band edges shift as a function of the width of the nanowires. The thinner nanowires (width= 5.4 nm) are metallic however the thicker nanowires (width= 22 nm) have sizable band gap. For thickest nanowires the size of the band gap is equal to the band gap of the terrace on which nanowires grow. In other words, as the nanowires get thicker a band gap opens up around the Fermi level. This indicates that there is a change in the structure of the nanowires as they grow wider. This structural change can be due to increased stress at the interface between nanowires and Si bulk or it could be a new phase of the Ir-silicide that forms. A similar trend has been reported before when at higher Ir coverage the semiconducting Ir_3Si_5 phase replaces $IrSi_2$ phase. Ir_3Si_5 crystallizes in the monoclinic structure (space group P21/c) with the following lattice constants: a = 6.406 Å b = 14.162 Å c = 11.553 Å β = 116.69°.[108] The origin and stability of the phase is attributed to its semi-coherent growth on Si substrate and non-hydrostatic plain strain. In addition to that a bulk phase of Ir_3Si_5 has been successfully grown before. Therefore, for nanowires beyond certain size the part of the nanowire above the surface can be in a semiconductor phase like Ir_3Si_5 or amorphous. This idea is actually supported by some of the TEM images we measured at ORNL. Figure 5.2e shows a TEM image of a cross section of a nanowire of approximately 18 nm wide. The part of the nanowire that grew into the bulk Si are well-defined crystals however above the surface the top left corner of the nanowire seems to have another crystal phase. The rest of the top portion of the nanowire looks amorphous.

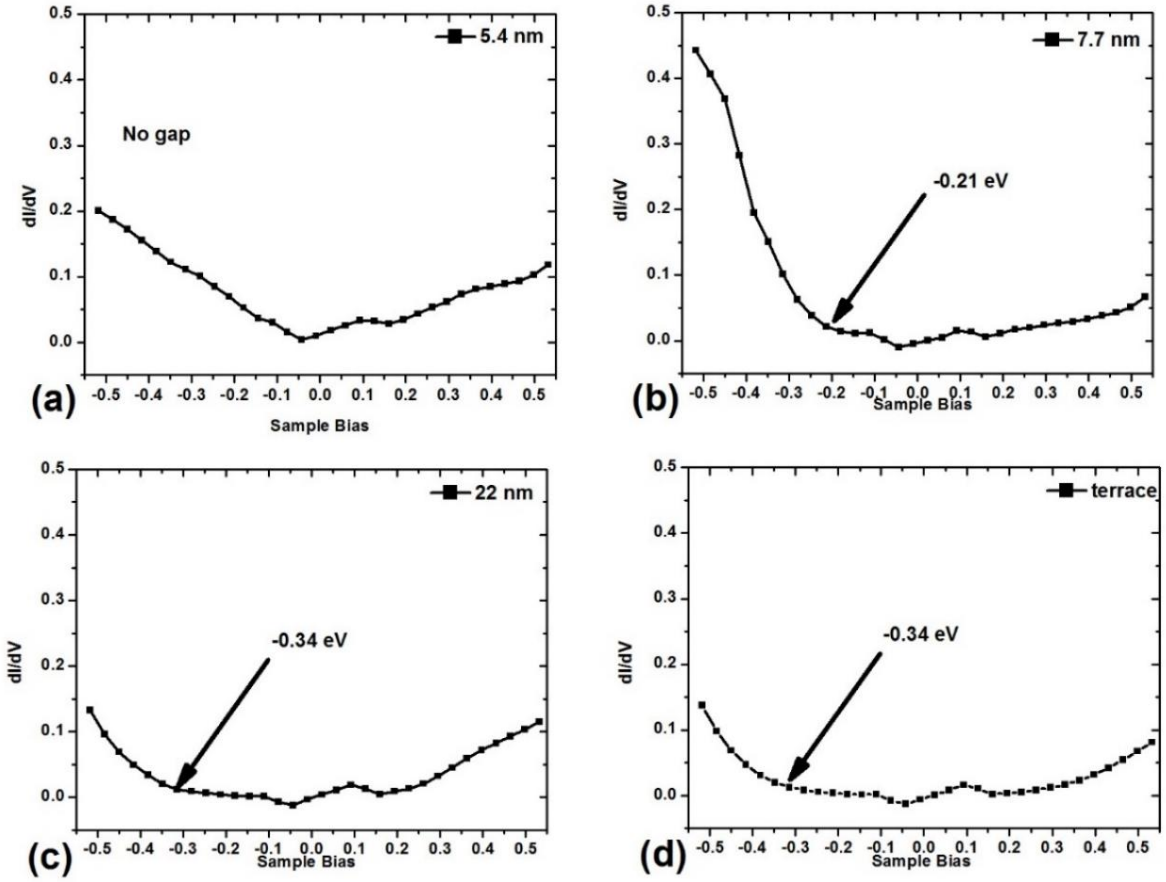

Figure 5.5 (a) (b) (c) and (d) are dI/dV curves calculated from the measured I(V) curves over nanowires with various widths. As the width of the nanowires grow wider the valence band edge moves away from the Fermi level.

5.4 Conclusion

In conclusion we performed HR-TEM measurements to investigate cross-section of Ir-silicide nanowires. Nanowires are mainly made of $IrSi_2$ which is metallic. However, dI/dV curves measured on wider nanowires showed that the nanowire has a band gap of about 0.34 eV which is approx. equal to the band gap of the terrace that the nanowires form. Ir_3Si_5 is the only semiconducting phase of Ir-silicides. Previous research on Ir grown on Si (001) surface has shown that for higher Ir concentrations it is possible to grow Ir_3Si_5 alongside of $IrSi_2$. We speculate that the wider nanowires have together with endotaxially grown $IrSi_2$ phase some Ir_3Si_5 and amorphous parts that grow above the surface.

CHAPETER VI

CONCLUSIONS

6.1 CONCLUSION

This dissertation investigates the structural and electronic properties of metal induced nanostructures on Si (110) surface. Among low index surfaces of Si, Si (110) is the least investigated and understood, probably because of its enormous and complex reconstructed unit cell. Difficult preparation technique of clean single domain Si (110)-``16×2" is also a reason this particular surface was not studied thoroughly. However, recently Si (110) surface has attracted a great deal of attention as MOSFET built on Si (110) has higher mobility than Si (100) or (111). Clean Si (110) "16×2" is a great template to grow nanostructure as it has inherent structural asymmetry. Nanostructures may exhibit exciting electronic and optical properties due to quantum confinement, which arises from their physical structure. For example, metal induced atomic chains can sometimes show 1D behavior in the band structure and their transport behavior is unique as electron cannot avoid each other. With the help of STM, XPS and TEM, Ir nanostructures on clean Si (110) were studied to reveal their atomic structures, electronic and chemical properties.

At the beginning of the project atomically clean Si (110) ``16×2" surface was obtained through high temperature flash-annealing and low temperature annealing. Upon confirmation of cleanliness and formation of well-ordered structure on Si (110) surface with STM, Ir was deposited in sub-ML regime to obtain nanowires. Nanowires on clean Si (110) were then investigated by STM/STS and TEM to reveal their structural and electronic properties. It is realized that the length and width of nanowires are coupled with each other and they can be grown up to ~ 100 nm in length along [001] direction with average width of ~ 21 nm but increasing Ir coverage makes nanowires wider. HRTEM images showed that for low coverage of Ir, nanowires were grown endotaxially and the crystal structure of the nanowires close to substrate were determined as $IrSi_2$ with the help of structural modelling in VESTA. Most importantly, STS measurements revealed that narrower nanowires are metallic but wider nanowires have band gap of ~ 0.34 eV.

When Ir coverage is increased up to 2 ML, the Si substrate surface is partially covered with flat terraces of Ir. High resolution STM images showed that terraces are covered with quasi periodic Ir quantum dots loosely bound to terrace as they can be moved by STM tip when tip is brought to their close vicinity. According to the STS measurements, both terraces and the quantum dots have metallic properties and QDs showed the Coulomb blockade and the negative differential resistance at the room temperature. The dI/dV curves measured on QDs showed opening of a Coulomb gap of 0.7 eV around the Fermi level which indicates that STM tip, QD and terrace forms a double junction system. XPS measurements show that the

interface between the Ir terrace and the Si substrate is made of Si rich silicide like $IrSi_{1.6}$ or $IrSi_3$.

In conclusion, Ir nanowires and quantum dots were successfully grown on clean and well-ordered Si (110)-``16×2" surface and they were characterized to reveal their unique structural and electronic properties which can be used for various electronic devices.

REFERENCES

[1] Somorjai GA, Li Y (2010) Introduction to Surface Chemistry and Catalysis (Wiley,Hoboken,NJ) 2nd Ed.

[2] Intel® 14 nm Technology, http://www.intel.com/content/www/us/en/silicon-innovations/intel-14nm-technology.html.

[3] Kenta Arima, Jun Katoh, Shinya Horie, Katsuyoshi Endo, Tomoya Ono, Shigetoshi Sugawa,Hiroshi Akahori, Akinobu Teramoto, and Tadahiro Ohmi. Hydrogen termination of Si (110) surfaces upon wet cleaning revealed by highly resolved scanning tunneling microscopy. *Journal of Applied Physics*, 98(10):103525, 2005.

[4] Zhian He, M. Stevens, David J. Smith, and P. A. Bennett. Dysprosium silicide nanowires on Si (110). *Applied Physics Letters*, 83(25):5292, 2003.

[5] S. Liang, R. Islam, David J. Smith, P. A. Bennett, J. R. OBrien, and B. Taylor. Magnetic iron silicide nanowires on Si (110). *Applied Physics Letters*, 88(11):113111, 2006.

[6] F.Jona:IBM J.Res.Develop.9(1965)375.

[7] Y. Yamato, Phys.Rev. B,50(1994).

[8] M. Setvın, V. Brazdova, K. Miki, and D. R. Bowler,Phys. Rev. B 82, 125421 (2010).

[9] A. Alguno, S. N. Filimonov, and M. Suemitsu, Surf. Sci. 605, 838 (2011).

[10] T. An, M. Yoshimura, I. Ono, and K. Ueda, Phys. Rev. B 61, 3006 (2000).

[11] A. A. Stekolnikov, J. Furthmuller, and F. Bechstedt, ¨ Phys. Rev. Lett. 93, 136104 (2004).

[12] A. A. Stekolnikov, J. Furthmuller, and F. Bechstedt, ¨ Phys. Rev. B 70, 045305 (2004).

[13] H. Ampo, S. Miura, K. Kato, Y. Ohkawa, and A. Tamura, Phys. Rev. B 34, 2329 (1986).

[14] T. Ichikawa, Surf. Sci. 544, 58 (2003).

[15] N. D. Kim, Y. K. Kim, C.-Y. Park, H. W. Yeom, H. Koh,E. Rotenberg, and J. R. Ahn, Phys.Rev. B 75, 125309 (2007).

[16] K. Sakamoto, M. Setvın, K. Mawatari, P. E. J. Eriksson, K. Miki, and R. I. G. Uhrberg, Phys.Rev. B 79, 045304 (2009).

[17] H. A. Atwater, A. Polman, "Plasmonics for improved photovoltaic devices" Nature Materials, 9, 205, (2010).

[18] S. A. Maier, M. L. Brongersma, P. G. Kik, S. Meltzer, A. A. G. Requicha, H. A. Atwater, "Plasmonics - A route to nanoscale optical devices" Advanced Materials, 13, 1501, (2001).

[19] U Banin, Y W Cao, D Katz, and O Millo, Nature (London) 400, 542 (1999); M A Reed, J N Randall, R J Aggarwal, R J Matyi, T M Moore, and A E Wesel, Phys. Rev. Lett. 60, 535 (1988).

[20] E.P.A.M Bakkers and D. Vanmaekelbergh, Phys. Rev. B 62, R7743 (2000).

[21] D Anselmetti, T Richmond, A Baratoff, G Borer, M Dreier, M Bernasconi, and H J Guntherodt, Europhys. Lett. 25, 297 (1994).

[22] T. Schmidth, R. J. Haug, K. V. Klitzing, A. Forster, and H. Luth, Phys. Lett. B 55, 2230 (1997).

[23] V. Lindberg and B. Hellsing, Journal of Physics: Condensed Matter 17, S1075 (2005).

[24] W. Cabanski, R. Koch, H. Mainer, G. Paler, J. Wendler, J. Ziegler, K. Hofmann, K. Eberhardt, P. Daimel, U. Prechtl, K. Kapser, "AEG PtSi modules: a summary" *Proc. SPIE.* 2746, 1996.

[25] A. Czernick, H. Palm, W. Cabanski, M. Schulz, U. Suckow, "Infrared photoemission of holes from ultrathin (3–20 nm) Pt/Ir-compound silicide films into silicon" *Appl. Phys. A*, 55, 180,1992.

[26] B.Y. Tsaur, M. M. Weeks, and P. W. Pellegrini, "Pt-Ir silicide Schottky-barrier IR detectors" IEEE *Electron Device Lett.* 9, 100, 1988.

[27] D. Hisamoto, W.C. Lee, J. Kedzierski, H. Takeuchi, K. Asano, C. Kuo, E. Anderson, T. J. King, F. J. Bokor, C. Hu, IEEE Transactions on Electronic Devices, 47, 2320, 2000.

[28] Y. P. Zhang, L. Yang, Y. H. Lai, G. Q. Xu, and X. S. Wang, Appl. Phys. Lett**.** 84, 401 (2004).

[29] H. Okino, I. Matsuda, R. Hobara, Y. Hosomura, S. Hasegawa, and P. A. Bennett, Appl. Phys.Lett. 86, 233108 (2005).

[30] A. Kida, H. Kajiyama, S. Heike, T. Hashizume, and K. Koike, Appl. Phys. Lett. 75**,** 540(1999).

[31] R. Losio, K. N. Altmann and F. J. Himpsel, Phys. Rev. Lett. 85**,** 808 (2000).

[32] J. R. Ahn, H. W. Yeom, H. S. Yoon, and I. -W. Lyo, Phys. Rev. Lett. 91, 196403 (2003).

[33] J. H. G. Owen, K. Miki, and D. R. Bowler, J. Mater. Sci. 41, 4568 (2006).

[34] Y. Chen, D. A.A. Ohlberg, G. Mederios-Ribario, Y. A. Chang, and R. S. Williams, Appl.Phys. Lett**.** 76, 4004 (2000).

[35] Y. Chen, D. A.A. Ohlberg, and R. S. Williams, J. Appl. Phys**.** 91**,** 3213 (2002).

[36] J. Nogami, B. Z. Liu, M. V. Katkov, C. Ohbuchi, and N. O. Birge, Phys. Rev. B 63, 233305(2001).

[37] O. Gurlu, O. A.O Adam, H. J.W. Zandvliet, and B. Poelsema, Appl. Phys. Lett. 83, 4610(2003).

[38] J. Wang, M. Li, and E. I. Altman, Phys. Rev. B 70**,** 233312 (2004).

[39] T. Sato, Y. Takeishi, H. Hara, Y. Okamoto, Phys. Rev. B, 4, 1950, (1971).

[40] A. Ciucivara, B. R. Sahu, S. Joshi, S. K. Banerjee, and L. Kleinman, Phys. Rev. B 75, 113309, (2007).

[41] Y. Liu, K. Ishii, T. Tsutsumi, M. Masahara, T. Sekigawa, K. Sakamoto, H. Takashima, H.Yamauchi, E. Suzuki, IEEE Trans. On Nanotechnology, 2, 198, (2003).

[42] S. Liang, R. Islam, D. J. Smith, P. A. Bennett, J. R. O'Brien, and B. Taylor, Appl. Phys. Lett. 88, 113111, (2006).

[43] Z. He, D. J. Smith, P. A. Bennett, Phys. Lett. 93, 256102, (2004).

[44] H. Okino, I. Matsuda, R. Hobara, Y. Hosomura, S. Hasegawa, P. A. Bennett, Appl. Phys. Lett. 86, 233108, 2005.

[45] Z. He, M. Stevens, D. J. Smith, P. A. Bennett, Appl. Phys. Lett. 83, 5292, 2003.

[46] S. M. Hus, H. H. Weitering, Appl. Phys. Lett. 103, 073101, 2013.

[47] Z. Q. Zou, G. M. Shi, L. M. Sun, X. Y. Liu, Appl. Phys. Lett. 113, 024305, 2013.

[48] J. A. Stroscio, R. M. Feenstra, A. P. Fein, Phys. Rev. Lett. 57, 2579, 1986.

[49] Y. Yamada, A. Girard, H. Asaoka, J. Phys. Conference Series, 100, 072018, 2008.

[50] T. An, M. Yoshimura, I. Ono and K. Ueda, Phys. Rev. B 61, 3006, 2000.

[51] T. Ichikawa, Surf. Sci. 544, 58, 2003.

[52] W. E. Packard, J. D. Dow, Phys. Rev. B 55, 15643, 1997.

[53] A. A. Stekolnikov, J. Furthmuller and F. Bechstedt, Phys. Rev. Lett. 93, 136104, 2004.

[54] A. A. Stekolnikov, J. Furthmuller and F. Bechstedt, Phys. Rev. B 70, 045305, 2004.

[55] "Data Analysis for Scientists and Engineers" Stuart L. Meyer, Peer Management Consultants, Ltd. September 1992.

[56] N.D. Kim, Y.K. Kim, C.-Y. Park, H.W. Yeom, H. Koh, E. Rotenberg, J.R. Ahn, Phys. Rev. B 75 (2007) 125309.

[57] K. Sakamoto, M. Setvin, K. Matawari, P. E. Eriksson, K. Miki, R. I. G. Uhrberg, Phys. Rev. B. 79, 045304, 2009.

[58] Introduction to Scanning Tunneling Microscopy, 2nd Ed. C. J. Chen, Oxford Univ. Press, New York, 2008.

[59] M. Setvín, V. Brázdová, D. R. Bowler, K. Tomatsu, K. Nakatsuji, F. Komor, K. Miki, Phys.Rev. B. 84, 115317, 2011.

[60] N. Oncel, D. Cakir, J. H. Dil, B. Slomski and G. Landolt, J. Phys. Cond. Matter, 26, 285501, 2014.

[61] D. Nicholls, N. Oncel, J. Phys. Cond. Matter, 25, 445004, 2013.

[62] R. N. Mohottige, N. Oncel, "Iridium–silicide nanowires on Si (110) surface", Surf. Sci. 641, 237, 2015.

[63] H. Roger, E. Hahn, H. Brune, J. -P. Bucker, K. Kern, "Building one- and two-dimensional nanostructures by diffusion-controlled aggregation at surfaces" Nature, 366, 141, 1993.

[64] J. Li, W.-D. Schneider, R. Berndt, S. Crampin, "Electron Confinement to Nanoscale Ag Islands on Ag(111): A Quantitative Study" Phys. Rev. Lett. 80, 3332, 1998.

[65] A. Carlsson, S. A. Lindgren, C. Svensson, L. Wallden, "Shifts and widths of metal-overlayer quantum-well states near E_F observed by photoemission" Phys. Rev. B 50, 8926, 1994.

[66] J. Kliewer, R. Berndt, "Scanning tunneling spectroscopy of Na on Cu (111)" Phys. Rev. B 65, 035412, 2001.

[67] A. Carlsson, B. Hellsing, S. A. Lindgren, L. Wallden, "High-resolution photoemission from a tunable quantum well" Cu (111)/Na Phys. Rev. B 56, 1593, 1997.

[68] O. Suekane, S. Hasegawa, M. Takata, T. Okui, H. Nakashima, "Scanning tunneling miscroscopy study of InAs islands grown on GaAs(001) substrates" Mater. Sci. Eng. B 88, 158, 2002.

[69] A. Madhukar, Q. Xie, P. Chen, A. Konkar, "Nature of strained InAs three-dimensional island formation and distribution on GaAs (100)" Appl. Phys. Lett. 64, 2727, 1994.

[70] G. S. Solomon, J. A. Trezza, J. S. Harris, "Substrate temperature and monolayer coverage effects on epitaxial ordering of InAs and InGaAs islands on GaAs" Appl. Phys. Lett. 66, 991, 1995.

[71] G. S. Solomon, J. A. Trezza, J. S. Harris, “Effects of monolayer coverage, flux ratio, and growth rate on the island density of InAs islands on GaAs” Appl. Phys. Lett. 66, 3161, 1995.

[72] H. Brune, “Microscopic view of epitaxial metal growth: nucleation and aggregation” Surf. Sci. Rep. 31, 121, 1998.

[73] A. Van der Ziel, “Noise in Solid Devices and Circuits”, Wiley New York, 1986.

[74] U Banin, Y W Cao, D Katz, and O Millo, Nature (London) 400, 542 (1999); M A Reed, J N Randall, R J Aggarwal, R J Matyi, T M Moore, and A E Wesel,” Observation of discrete electronic states in a zero-dimensional semiconductor nanostructure” Phys. Rev. Lett. 60, 535 (1988).

[75] E.P.A.M Bakkers and D. Vanmaekelbergh, “Resonant electron tunneling through semiconducting nanocrystals in a symmetrical and an asymmetrical junction” Phys. Rev. B 62, R7743 (2000).

[76] D Anselmetti, T Richmond, A Baratoff, G Borer, M Dreier, M Bernasconi, and H J Guntherodt, Single-Electron “Tunnelling at Room Temperature with Adjustable Double-Barrier Junctions” Europhys. Lett. 25, 297 (1994).

[77] T. Schmidth, R. J. Haug, K. V. Klitzing, A. Forster, and H. Luth, “Single-electron transport in small resonant-tunneling diodes with various barrier-thickness asymmetries” Phys. Rev. B 55, 2230 (1997).

[78] V. Lindberg and B. Hellsing, “Metallic quantum dots” Journal of Physics: Condensed Matter 17, S1075 (2005).

[79] C.A. Neugebauer and M.B. Webb, “Electrical Conduction Mechanism in Ultrathin, Evaporated Metal Films” J.Appl.Phys. 33, 74 (1962).

[80] D. K. Ferry and S. M. Goodnick, Transport in Nanostructures (Cambridge University Press, Cambridge, 1997).

[81] J. A. Stroscio, R. M. Feenstra, A. P. Fein, “Electronic Structure of the Si(111)2 × 1 Surface by Scanning-Tunneling Microscopy” Phys. Rev. Lett. 57, 2579, 1986.

[82] D. Briggs and M. P. Seah. Practical surface analysis, Willey, New York (1983).

[83] A. E. Hanna, M. Tinkham, “Variation of the Coulomb staircase in a two-junction system by fractional electron charge” Phys. Rev. B, 44, 5919, 1991.

[84] E. Puppin, I. Lindau, I. Abbati, “Photoemission core level shifts in Gd silicides” Solid State Commun. 77, 983, 1991.

[85] M. Wittmer, P. Oelhafen, and K. N. Tu. “Electronic structure of iridium silicides” Phys. Rev. B 33, 5391 (1986).

[86] S.J. Morgan, R.H. Williams, and J.M. Mooney. “An XPS study of thin Pt and Ir silicide overlayer formation on Si (100)2 X 1 surfaces” Appl. Surf. Sci. 56, 493 (1992).

[87] G. Larrieu, E. Dubois, X. Wallart, and J. Katcki. “Kinetics, stoichiometry, morphology, and current drive capabilities of Ir-based silicides” J. Appl. Phys. 102, 094504 (2007).

[88] M. Peuckert, Electrochim. Acta, “XPS investigation of surface oxidation layers on a platinum electrode in alkaline solution” 29, 1315, 1984.

[89] D. Hisamoto, W.C. Lee, J. Kedzierski, H. Takeuchi, K. Asano, C. Kuo, E. Anderson, T. J. King, F. J. Bokor, C. Hu, IEEE Transactions on Electronic Devices, 47, 2320, 2000.

[90] Y. P. Zhang, L. Yang, Y. H. Lai, G. Q. Xu, and X. S. Wang, Appl. Phys. Lett. 84**,** 401 (2004).

[91] H. Okino, I. Matsuda, R. Hobara, Y. Hosomura, S. Hasegawa, and P. A. Bennett, Appl. Phys. Lett. 86, 233108 (2005).

[92] A. Kida, H. Kajiyama, S. Heike, T. Hashizume, and K. Koike, Appl. Phys. Lett. 75, 540 (1999).

[93] R. Losio, K. N. Altmann and F. J. Himpsel, Phys. Rev. Lett. 85, 808 (2000).

[94] J. R. Ahn, H. W. Yeom, H. S. Yoon, and I. -W. Lyo, Phys. Rev. Lett. 91, 196403 (2003).

[95] J. H. G. Owen, K. Miki, and D. R. Bowler, J. Mater. Sci**.** 41, 4568 (2006).

[96] Y. Chen, D. A.A. Ohlberg, G. Mederios-Ribario, Y. A. Chang, and R. S. Williams, Appl. Phys. Lett. 76, 4004 (2000).

[97] Y. Chen, D. A.A. Ohlberg, and R. S. Williams, J. Appl. Phys. 91**,** 3213 (2002).

[98] J. Nogami, B. Z. Liu, M. V. Katkov, C. Ohbuchi, and N. O. Birge, Phys. Rev. B 63**,** 233305 (2001).

[99] O. Gurlu, O. A.O Adam, H. J.W. Zandvliet, and B. Poelsema, Appl. Phys. Lett. 83**,** 4610 (2003).

[100] J. Wang, M. Li, and E. I. Altman, Phys. Rev. B 70**,** 233312 (2004).

[101] A. Ciucivara, B. R. Sahu, S. Joshi, S. K. Banerjee, and L. Kleinman, Phys. Rev. B 75, 113309, (2007).

[102] Y. Liu, K. Ishii, T. Tsutsumi, M. Masahara, T. Sekigawa, K. Sakamoto, H. Takashima, H. Yamauchi, E. Suzuki, IEEE Trans. On Nanotechnology, 2, 198, (2003).

[103] S. Liang, R. Islam, D. J. Smith, P. A. Bennett, J. R. O'Brien, and B. Taylor, Appl. Phys. Lett. 88, 113111, (2006).

[104] Z. He, D. J. Smith, P. A. Bennett, Phys. Lett. 93, 256102, (2004).

[105] H. Okino, I. Matsuda, R. Hobara, Y. Hosomura, S. Hasegawa, P. A. Bennett, Appl. Phys. Lett. 86, 233108, 2005.

[106] Z. He, M. Stevens, D. J. Smith, P. A. Bennett, Appl. Phys. Lett. 83, 5292, 2003.

[107] S. M. Hus, H. H. Weitering, Appl. Phys. Lett. 103, 073101, 2013.

[108] Q. Zou, G. M. Shi, L.M. Sun, X.Y. Liu, Appl. Phys. Lett. 113, 024305, 2013.